

## Starcunts Redivivus. IV. Density Laws Through Photometric Parallaxes

M. H. Siegel<sup>1,4</sup>, S. R. Majewski<sup>1,2,3</sup>,  
 I. N. Reid<sup>2,4</sup>,  
 and I. B. Thompson<sup>5</sup>

### ABSTRACT

In an effort to more precisely define the spatial distribution of Galactic field stars, we present an analysis of the photometric parallaxes of stars in seven Kapteyn Selected Areas. Our photometry database covers  $\sim 14.9$  square degrees and contain over 130,000 stars, of which approximately 70,000 are in a color range ( $0.4 \leq R - I \leq 1.5$ ) for which relatively unambiguous photometric parallaxes can be derived. We discuss our photometry pipeline, our method of determining photometric parallaxes and our analysis efforts. We also address the affects of Malmquist Bias, subgiant/giant contamination, metallicity and binary stars upon the derived density laws. The affect of binary stars is the most significant of these biases – a binary star fraction of 50% could result in derived scale heights that are 80% of the actual values.

We find that while the disk-like populations of the Milky Way are easily constrained in a simultaneous analysis of all seven fields, no good simultaneous solution for the halo is found. We have applied halo density laws taken from other studies and find that the Besançon flattened power law halo model ( $\frac{c}{a} = 0.6, \rho \propto r^{-2.75}$ ) produces the best fit to our data. With this halo, the thick disk has a scale height of 750 pc with an 8.5% normalization to the old disk. The old disk scale height is  $\sim 280$ -300 pc for our early type ( $5.8 \leq M_R < 6.8$ ) dwarfs and rises to  $\sim 350$  pc for our late type ( $8.8 \leq M_R \leq 10.2$ ) dwarf stars. Corrected for a binary fraction of 50%, these scale heights are 940 pc and 350-375 pc, respectively.

Even with this model, there are systematic discrepancies between the observed and predicted density distributions – discrepancies only apparent at the faint magnitudes reached by our survey. Specifically, our model produces density overpredictions in the inner Galaxy and density underpredictions in the outer Galaxy. A possible escape

---

<sup>1</sup>Department of Astronomy, University of Virginia, Charlottesville, VA, 22903 (mhs4p@virginia.edu, srm4n@didjeridu.astro.virginia.edu)

<sup>2</sup>Visiting Research Associate, The Observatories of the Carnegie Institution of Washington, 813 Santa Barbara Street, Pasadena, CA 91101

<sup>3</sup>David and Lucile Packard Foundation Fellow

<sup>4</sup>Space Telescope Science Institute, 3700 San Martin Drive, Baltimore, MD 21218 (msiegel@stsci.edu, inr@stsci.edu)

<sup>5</sup>The Observatories of the Carnegie Institution of Washington, 813 Santa Barbara Street, Pasadena, CA 91101 (ian@ociw.edu)

from this dilemma is offered by modeling the stellar halo as a two-component system, as favored by studies of BHB/RR Lyrae stars and recent analyses of the kinematics of metal-poor stars. In this paradigm, the halo has a flattened inner distribution and a roughly spherical, but substructured outer distribution. Further reconciliation could be provided by a flared thick disk, a structure consistent with a merger origin for that population.

*Subject headings:* Galaxy: Structure, Galaxy: halo, Galaxy: stellar content, Galaxy: formation, Stars: colors, Stars: magnitudes

## 1. Introduction

The present stellar content of the Milky Way is a fossil record of its formation and evolution. When a star is formed, its kinematical and chemical properties reflect the state of the Galaxy at that location at the time of the star’s formation. In high density chaotic regions of the Galaxy – such as the Galactic midplane – that information can be quickly scrambled. In the more remote regions of the Galaxy, the story told by ancient stars is still legible. Since lower-mass stars have lifetimes of order a Hubble time or greater, they remain in the Galaxy as echoes of the its distant past. The most sensible and efficient strategy for reading the messages contained in old stars is to ascertain the bulk properties of stars grouped together by similar characteristics, i.e. stellar populations.

The division of Galactic field stars into distinct populations was greatly clarified by Baade’s (1944) division of stars into Population I and Population II. This system was expanded into five populations in the seminal 1957 Vatican conference (O’Connell 1958). Even after nearly six decades of work, however, there is still some uncertainty on the exact characteristics of each population and, more importantly, what those characteristics tell us about the evolution of the Galaxy. Indeed, there is not even a consensus on *how many* populations are required to fully describe the Milky Way and whether distinct populations remain a sensible paradigm (see reviews in Majewski 1993, 1999a).

This series’ first contribution to the debate (Reid & Majewski 1993, hereafter Paper I) used photographic starcounts data to derive an interim model for the spatial distribution of field stars toward the Galactic poles. Our second (Reid et al. 1996, hereafter Paper II) investigated small but extremely deep data sets to apply constraints to the halo luminosity function. A later contribution (Majewski et al. 1997, hereafter Paper III) investigated an anomalous starcounts signature discovered in starcount data not presented here, and explored the possibility of contamination of our starcount data by streams of stars tidally stripped from the Sagittarius dSph galaxy.

The present discussion is a more complete and sophisticated investigation of a number of Kapteyn Selected Areas using large area, CCD-based datasets. §2 details the general characteristics

of this dataset, while §3 and §4 detail the photometry pipeline and object classification methods, respectively. We then use a subset of this data and the method of photometric parallax to apply stronger global constraints to the spatial distribution of Galactic field stars than any previous starcounts survey has been capable of. §5 details our method of photometric parallax, §6-8 cover the analysis of the starcounts and our attempt to fit a self-consistent model to the data in all seven fields and §9 discusses the implication of those results. §10 summarizes the primary results of this endeavor.

## 2. Observational Program

### 2.1. Overview

The statistical foundation of starcounts rests in the Von Seeliger’s (1898) Fundamental Equation of Stellar Statistics. Expanded to include stellar colors, this equation may be written as:

$$A(m_V, S_{B-V}) = \sum A_i(m_v, S_{B-V}) = \Omega \sum \int_0^{R_{max}} \Phi_i(M, S) D_i(r) r^2 dr \quad (1)$$

in which  $A$  is the differential number of counts at any particular magnitude and color,  $A_i$  is the contribution to those counts from population  $i$ ,  $\Omega$  is the solid angle observed,  $\Phi_i$  is the luminosity function of population  $i$  and  $D_i$  is the density distribution of population  $i$ . In this formulation, the number of counts at a given color and magnitude is the sum over the stellar populations of the convolution of the luminosity and density distribution functions. Deriving scientific results from starcounts is difficult because the starcounts equation is not invertable. Because of the non-invertability and the vagaries of solving the non-unique convolution by trial and error, starcounts *by themselves* are in general a weak tool for exploring the Galaxy. In combination with a small amount of external information, however, they can become a potent implement.

The non-uniqueness problem is perhaps demonstrated by the breadth of Galactic structure models that have been derived from starcount studies, as listed in Table I. While the derived structural parameters for the thin disk occupy a fairly narrow range of values, the density law of the thick disk <sup>6</sup> (Intermediate Population II or IPII in the Vatican Conference nomenclature) is less certain, with a large range of values as illustrated in Figure 1. Although there appears to be a cluster of results in Figure 1, this may be a selection effect. The tabulated studies have often explored similar data sets with similar limitations. In fact, several of them probe the same direction in the sky (the Galactic poles, especially the North Galactic Pole). It is perhaps encouraging that they produce similar results for one direction of sky. It should be noted that there is still debate over whether the thick disk is, in fact, a distinct population or is just an

---

<sup>6</sup>We succumb to the pressure of popular use of the term “thick disk” in this paper, despite potential implications for the structure and origin of this population that may inadvertently be implied by this expression.

extended tail of the old disk. However, as far as the halo is concerned, the results from starcount surveys span almost the entire range of parameter space from flattened de Vaucouleurs spheroids (Wyse & Gilmore, 1989; Larsen 1996, hereafter L96) to perfectly spherical power law distributions (Ng et al. 1997, hereafter N97).

As part of a campaign to obtain photometry, spectroscopy and proper motions for stars in a large number of the Kapteyn Selected Areas, we have collected a set of photometric imaging data suitable for starcounts analyses. These data are notably superior to previous efforts and are of high enough quality to provide a critical check on the early results from SDSS as presented, for example, in Chen et al. 2001 (hereafter C01). The specific advantages of our starcounts program are:

1. *Multiple lines of sight.* An over-reliance upon data taken in a few directions in the sky is characteristic of much of the prior starcounts literature. Most studies have focused upon one or a few directions in the sky generally in either tiny areas to great depth (e.g, Paper I, Paper II) or over a large area to shallower depth (e.g. Gilmore & Reid 1983, hereafter GR83). Only a few programs have attempted to survey the Galaxy in multiple directions. Chief among those are the Basel Halo Program (most recent contribution by Buser et al. 1999, hereafter B99), which has been examining program fields with photographic plates for some four decades; the Besançon program (e.g. Robin et al. 1996, hereafter R96), which attempts to use population synthesis to analyze data from their own program fields as well as previous starcount studies; the APS-POSS program (L96), the most extensive survey to date; and the Sloan Digital Sky Survey (SDSS), which has recently published its first analysis (C01).

As noted in Paper I and in R96, evaluation of starcounts in a single direction can lead to degenerate density law solutions. In addition, surveys that only probe at the Galactic poles (in Figure 1 this includes GR83, Gilmore 1984, Robin & Creze 1986, Yoshii et al. 1987, Kuijken & Gilmore 1989, Paper I, N97) are completely insensitive to radial terms in the population distributions. The photometry program presented here consists of eleven Kapteyn Selected Areas plus one additional area. Table II lists the observed fields and Figure 2 shows an Aitoff projection of their distribution across the Galaxy. These fields cover the South Galactic Pole, the Galactic anti-center, the  $90^\circ - 270^\circ$  meridional slice and locations  $40^\circ$  above and below the Galactic Center.

2. *Completeness to faint magnitudes.* The average photometric depth of our data is  $V \sim 21.4$  and a substantial portion image to  $V \sim 22$ , a depth comparable to the deepest moderate area surveys conducted thus far (Paper I; Robin et al. 2000, hereafter R00; C01) and significantly deeper than the large surveys of L96, R96 or B99. While we can not match the deepest starcount surveys, such as those from the Hubble Deep Field and Flanking Fields (Méndez & Guzman 1998; Paper II) or SA 57 (Paper I), those surveys have covered only a single direction of sky and/or a very small solid angle with a commensurately low number of stars. Even the multi-directional HST-based survey of Zheng et al. (2001) has an average of only 10 stars per pointing. Deep wide field starcounts can be extracted from galaxy count surveys (see, e.g., Phleps et al. 2000). Deeper

surveys, however, run into two limitations. Star-galaxy separation grows increasingly important, but increasingly difficult, at fainter magnitudes. In fact, it may be impossible to distinguish accurately between stars and galaxies in a ground-based survey much fainter than  $V \sim 22.5$  except with data from large-aperture telescopes with fine plate scales observed under exceptional seeing conditions. This problem is more significant for studies of stars than for galaxies because the latter far outnumber the former at faint ( $V > 22$ ) magnitudes. A second complication is the low sensitivity of starcounts to the parameters of the halo. Because of the large volume over which halo stars are spread, stringent constraints are difficult to apply. Thus deeper surveys will not necessarily produce superior results (see Paper II and Reid et al. 1998 for a discussion of both of those problems).

3. *Linear photometry over a large dynamic range.* Most of the previous surveys (all of those listed in Table I with the exception of N97 and C01) have derived their results from studies of photographic plates. While photography has the distinct advantage of imaging a large section of sky in a single observation, the non-linearity of the medium requires careful calibration by photometric standards. The fraction of counts contributed by each population is a function of magnitude and thus any error in calibration will manifest itself as a bias in the derived density laws. Additionally, the large dynamic range of our data ( $12 \leq V \leq 22$ ) provides a significant advantage over purely deep surveys, such as those using HST, that can only probe the most distant stars in the Galaxy. Gizis & Reid (1999), for example, have shown that HST-based halo luminosity functions are discrepant from ground-based studies possibly because of the inability of deep surveys to probe the nearby Galaxy.

4. *Sky coverage.* One of the most important aspects of a starcounts survey is area. The greater the area surveyed, the less the data are sensitive to small density fluctuations in the Galaxy. We observed the Selected Areas in our study over 1.5-2.5 square degrees each. The only CCD-based study that exceeds this coverage is C01, which covers 279 deg<sup>2</sup>. Our survey is much more extensive than previous CCD surveys, such as R00 (1.4 deg<sup>2</sup>), Paper II (0.0124 deg<sup>2</sup>) and Zheng et al. ( $\sim 0.2$  deg<sup>2</sup>). Several photographic studies (e.g., L96, GR83) cover larger areas.

5. *Homogeneity.* Many of the difficulties listed above can be overcome by combining multiple data sets. R96 and R00 approach starcounts with this method. Those studies, however, specifically note the lack of homogeneity as a potential problem, with possible discrepancies in the apparent starcounts from field to field. Indeed, they note that there are discrepancies among different studies of the *same* fields. Our data are taken through the same telescope with the same combination of filters, calibrated to the same standards and reduced through the same pipeline.

While our survey may be inferior to others in any particular aspect, the *combination* of the above advantages gives our study a view of the Galaxy that is only matched by C01. Even the latter surveys an area (an SDSS strip) not necessarily optimized for constraining density laws for all stellar populations, although this sensitivity will grow as SDSS covers more of the sky. Another comparable survey is the APS-POSS survey (L96), which covers 1440 square degrees in ninety

directions over the magnitude interval  $12 < O < 20$  and with careful photoelectric calibration to remove the non-linearity inherent to the photographic plates. Although APS-POSS lacks the depth of our study or C01, these shortcomings are compensated for to some extent by the sheer volume of stars surveyed (a staggering 2.6 million stars of the nearly  $10^9$  available from the POSS).

So far, this discussion has focused on optical starcounts. Much progress may be made in the analysis of infrared starcounts, now available from the 2MASS program, which covers the entire sky with a homogenous data sample. Because 2MASS can dramatically reduce the effect of interstellar reddening, NIR starcounts will be valuable at low Galactic latitudes, where they can reach all the way to the opposite side of the Galaxy. 2MASS's primary limitation is a rather shallow magnitude limit (see, e.g. Beichman et al. 1998) and the extremely narrow NIR color range of K- and M-type stars, which limits sensitivity to spectral type.

In summary, our study has sufficient depth and number of stars to probe the density laws from the nearby thin disk to the distant halo. We also have the range in latitude and longitude to break the apparent normalization-scale height degeneracy problem described in Paper I.

## 2.2. Observations

We observed twelve fields over the course of nine observing runs from August 1993 through September 1997 with the Las Campanas Swope 1-meter telescope. These observing runs spanned a total of 51 nights, 31 of which were photometric. From August 1993 through January 1995, we used the 2048<sup>2</sup> Tektronix 3 CCD camera at Cassegrain focus with a pixel scale of 0''.61 per pixel. In September of 1995, we switched to the larger pixelated (0''.69 per pixel) and more sensitive Tektronix 5 CCD chip. The last observing run used the SITe 1 CCD chip, a near twin of the Tektronix 5. While data from all three chips have been reduced through the pipeline described in §2-4, the subsample used for this particular study is entirely from the Tek 5 and SITe 1 chips.

Each Selected Area was divided into a grid of subfields. These grids were designed to provide maximum spatial coverage of the Selected Area while allowing a small overlap with adjacent subfields for photometric comparison or bootstrap calibration of non-photometric observations. The fields were first observed in Johnson *BV* and Thuan-Gunn *i* filters. After the switch to Tek 5, the Cousins *R* filter was added to the program. Both the *B* and *R* filters were of the Harris prescription. A number of subfields were also observed with the *CuSO*<sub>4</sub> or Harris *U* band filter. All of these passbands were calibrated to the Landolt (1992) system (see §3.2) which uses Johnson *UBV* and Cousins *RI* filters. Color terms in the transformations (see below) removed discrepancies between our observational photometry system and Landolt's standard system.

Each subfield in the grid was observed in a sequence of *BVI*, *RI*, *BVRI* or *UB* exposures. Long and short exposures were obtained in each filter to increase the dynamic range of the sample. Short exposures were 15-40 seconds, depending on observing conditions and filter. Long exposures were typically 450-1200 seconds. This provided photometric coverage to an estimated average depth

of  $(B, V, R, I) = (21.1, 21.4, 21.5, 20.6)$  with stars as faint as  $(B, V, R, I) = (23.0, 22.6, 22.2, 21.5)$  photometered in our best frames. The  $U$  band observations proved particularly difficult and exposure times as great as 1800 seconds were sometimes required to reach our target photometric depth. These frames have not yet been thoroughly evaluated to test their photometric depth but preliminary indications are that they are complete to  $U \sim 21$ . Tek 5  $BVI$  observations typically reach a magnitude fainter than the Tek 3  $BVI$  observations.

In July of 1996, we observed two additional fields to constrain asymmetry across the  $l = 0^\circ$  meridian. These fields were similar in coordinates to SA184 and SA107 but reflected across the Galactic meridian (and thus these “anti-fields” were given the labels ASA184 and ASA107). In July of 1997, we observed subfields three and eight of ASA184 with the 2.5 meter du Pont telescope at Las Campanas in an attempt to determine if those fields may be contaminated by the tidal stream of the Sagittarius dSph (described in Paper III). The 2.5 meter telescope, in addition to having larger aperture, boasts a finer plate scale than Swope. Thus, a side benefit of the exploration was the provision of two deep exposures with which to compare our program observations and to evaluate directly our completeness level and classification success (§4.3).

### 3. Photometric Pipeline

#### 3.1. Reductions

The CCD images were trimmed and corrected for bias, overscan, flat field and illumination effects with the CCDRED package in IRAF.<sup>7</sup> We found that the best illumination correction was produced by using the DIMSUM package to mask bright stars in our deeper program exposures and then using these masked images as additional sky images to combine into sky flats. We used the IMREPLACE process of IRAF to mask bad pixels to typical sky values.

We performed photometry on the data using the IRAF version of the DAOPHOT photometry package (Stetson 1987). A Moffat profile was used with quadratic geometric variation. The Swope data proved to be an excellent source of wide field photometry. Typical DAOPHOT  $\chi$  values of the PSF fit were 0.01-0.03, with few frames worse than 0.04. Visual inspection of the frames revealed star subtraction to be excellent.

The fields observed in our program are uncrowded and one could argue that simple aperture photometry would be adequate. We have found, however, that the structural parameters produced by DAOPHOT are useful for object classification (see §4). We have also found that aperture photometry is noticeably inferior to PSF photometry at the faint end of the data. Finally, PSF photometry can interpolate around chip edges and bad pixels (a significant problem with the Tek

---

<sup>7</sup> IRAF is distributed by the National Optical Astronomy Observatories, which are operated by the Association of Universities for Research in Astronomy, Inc., under cooperative agreement with the National Science Foundation.

3 chip) to render a more complete survey.

### 3.2. Frame Matching, Calibration and Photometric Consistency

During our observing runs, we periodically observed Landolt (1992) standard stars with a broad color range over a large range of airmasses. In addition, more than half of our survey areas contain Landolt standard stars. The raw photometry was calibrated onto the standard system through several steps. We first derived transformation constants for each observing run, using the formulation:

$$\begin{aligned}
 U &= m_u + u1 + i2 \times X_u + u3 \times (U - B) + u4 \times (U - B) \times X_u + u5 \times (U - B)^2 \\
 B &= m_b + b1 + b2 \times X_b + b3 \times (B - V) + b4 \times (B - V) \times X_b + b5 \times (B - V)^2 \\
 V &= m_v + v1 + v2 \times X_v + v3 \times (B - V) + v4 \times (B - V) \times X_v + v5 \times (B - V)^2 \\
 R &= m_r + r1 + r2 \times X_r + r3 \times (R - I) + r4 \times (R - I) \times X_r + r5 \times (R - I)^2 \\
 I &= m_i + i1 + i2 \times X_i + i3 \times (R - I) + i4 \times (R - I) \times X_i + i5 \times (R - I)^2
 \end{aligned}$$

where, in the visual passband,  $V$  is the apparent magnitude,  $m_v$  is the instrumental magnitude,  $B - V$  is the color and  $X_v$  is the airmass of the observation; corresponding terms apply to the other four passbands. These equations were solved via the matrix inversion technique described by Harris (1981) through a program that allows the user to fit one of the above equations interactively. For all five filters, the color-squared and color-airmass terms were found to be insignificant and were subsequently dropped from the solution with no loss of precision or accuracy. Solutions converged at better than 0.03 magnitudes RMS precision in all five passbands for all photometric nights. Most solutions were better than 0.01 magnitudes.

Our ultimate goal was for each Selected Area photometry catalogue to be mosaiced from photometrically interlocked subfields and calibrated to the Landolt system. The first step was to combine the multifilter data for each subfield into a calibrated photometry catalogue. The multifilter data were matched using the DAOMASTER code included with DAOPHOT. These instrumental subfield catalogues were then transformed to the standard system using the equations above and a program designed to resolve any zero point differences between multiple observations in the same passband. The photometry from each image was compared to the average of all photometric images in its passband. The resulting zero point difference was then added to the  $v1$  term. This process was performed iteratively until the frame-to-frame residuals were reduced below a user-specified level (usually .001 magnitudes) in each passband. Non-photometric observations were included in the solution and were correctly transformed to the average photometry of the photometric frames (see below). Once zero point differences were removed, the magnitudes were averaged to produce the final measure. Typical zero point difference were a few hundredths of a magnitude.



The next step was to interlock the photometry by comparing overlapping photometric subfields. We found systematic zero point residuals of 0.01-0.1 magnitudes, possibly resulting from changes in sky transparency or variations in the extinction coefficients.

A number of subfields had only non-photometric observations. To calibrate these subfields, we used the stars at the edge of the images that overlapped photometric subfields for bootstrap calibration. Direct comparison allowed the calculation of a separate zero point term for each CCD frame. Color terms were then set to the values derived for the observing run on which the non-photometric frame was taken. The bootstrap calibrations showed no sign of non-linearity in magnitude or color.

Once these residuals were corrected for, we identified Landolt standard stars within each Selected Area and compared our final photometry with the Landolt measures to identify any remaining zero point problems. The residuals of these comparisons are within the expected photometric scatter across the magnitude range (see Figure 3) and the average residual of standard stars within any particular Selected Area is within the stated photometric error.

Astrometry for our stars was derived from the USNO SA2.0 catalogue (Monet et al. 1986) using the STSDAS TFINDER package. The subfield catalogues were then combined using this astrometry to match the stars. The *RI* data utilized for the photometric parallax program discussed below do not have multiply observed stars removed (i.e., stars at the edge of each CCD chip, about 25% of the sample). To account for this effect upon our analysis, we have calculated the solid angles below as though the subfields did not overlap. In a statistical survey, the effect on the analysis is negligible because multiply-represented stars appear only as a function of their location within each mosaiced SA field. Future contributions will be from a catalogue with the multiples averaged together.

#### 4. Completeness and Classification

The analysis of deep starcounts can be critically affected by faint galaxy contamination (see Paper I for discussion). At the magnitude limit of our data ( $R \sim 21$ ), galaxies outnumber stars by an order of magnitude. Because extragalactic objects are distributed uniformly over the sky and are predominantly faint, failure to fully remove this source of contamination will, for example, skew evaluations of the distant halo density distribution toward high axial ratios (i.e., a rounder halo) and shallow density gradients.

As shown in Paper II, photometric information alone is rather ineffective at discriminating stars from galaxies. Approximately two thirds of galaxian objects lie within  $2\sigma$  of the stellar locus in multicolor space. This is hardly surprisingly since galaxies are, after all, comprised of stars. Morphological information has proven to be the single best discriminant and Paper II identified four morphological classification methods – ellipticity, the  $\chi$  parameter of DAOPHOT, and two measures of image compactness – with which to separate stars from galaxies.

Those methods, though effective, were designed for a small set of HST and Keck observations and may not be as effective for data taken at a much coarser pixel scale ( $0''.61 - 0''.69$  per pixel). Moreover, the extensive data set produced by our program demands more automated methods. The DAOPHOT program produces enough information to provide reasonable object classification. The DAOFIND algorithm uses estimates of roundness and sharpness to filter the initial list of potential stars. Additionally, ALLSTAR produces measures of  $\chi$  and SHARP. We have used these measured to construct a simple but effective classification engine.

Figure 4 shows the morphological parameters of objects in a typical field as a function of magnitude. Brighter than a certain magnitude, there are clearly two loci of objects corresponding to stars and galaxies. The magnitude at which the loci merge is the faintest magnitude at which we can confidently discriminate stars from galaxies. All objects fainter than this classification limit must be considered potentially misclassified.

Since our analysis is limited to objects brighter than the classification limit, the classification limit replaced the magnitude limit in our evaluation of survey completeness. Of course, the classification limit and the magnitude limit of any particular CCD frame should be correlated since the factors that limit successful image classification - seeing, sky brightness, pixel scale - are also those which affect photometric depth.

Our technique for star/galaxy separation was to inspect the magnitude- $\chi$  and magnitude-SHARP distribution of each subfield to identify the classification limit. Objects below this limiting magnitude were selected as stars if they had  $\chi < 2$  and  $-0.4 < SHARP < S_u$ , where  $S_u$  is the value of SHARP where the galaxian and stellar loci merge<sup>8</sup>.  $S_u$  varied from image to image depending on observing conditions but was typically 0.1-0.15. DAOFIND parameters were left at the IRAF defaults of  $-1 < ROUND < 1$  and  $0.2 < SHARP < 1.0$ . This technique was the product of extensive testing of the data pipeline using the methods detailed below.

#### 4.1. ADDSTAR

Our first pipeline test used the DAOPHOT task ADDSTAR to implant a set of 1000 artificial stars, evenly distributed between  $V = 15$  and  $V = 25$ , to eight sets of Tek 3 and Tek 5 observations of varying quality. This program adds stellar images to the CCD frame by scaling the PSF to the appropriate magnitude and adding realistic noise. The revised CCD images were photometered and classified, after which the artificial stars were extracted. Figure 5a shows the combined result of this test before object classification. We recover 100% of the stars to

---

<sup>8</sup>Although a more stringent  $\chi$  limit would be reasonable, we found that some bright stars had elevated  $\chi$  values, possibly a result of DAOPHOT underestimating the expected error or nonlinearity near the saturation limit of the CCD. We therefore used a more generous upper limit. The galaxies allowed by this generous  $\chi$  limit at the faint end are removed by the more stringent SHARP limit.

and beyond the classification limit of each frame. The recovered fraction reaches the 50% level approximately 1.5 magnitudes fainter than the classification limit and the 0% level 3 magnitudes below the limit. This result is independent of the actual value of the imaging limit and consistent from the worst data (bright sky background,  $> 2''.5$  seeing) to the best data (low sky background,  $1''.0$  seeing). Figure 5b shows the result of a high resolution version of this test, in which we added 1000 stars in a 3-magnitude wide bin centered on the classification limit. We find that the recovered fraction is still 100% at the classification limit, dropping off to the 50% level 1.2 magnitudes fainter.

We then ran the extracted measures through the classification pipeline to determine how many artificial stars were misclassified as galaxies. Figure 6 shows retained fraction as a function of magnitude with respect to the classification limit. We have found that our method leaves the artificial stars 96-100% intact. The percentage of stars misclassified appears to be independent of magnitude above the classification limit. Even the high resolution data show, at most, a drop from 99% to 96% in the recovered fraction to the classification limit.

The measured photometry of our artificial stars has unrealistically small errors, producing unrealistically low  $\chi$ 's. This results from the analytical PSF being only an approximation to the light distribution of real stars, but is a perfect description of artificial stars. Figure 7 shows the distribution of the artificial stars in magnitude- $\chi$  and magnitude-SHARP space, which can be contrasted with Figure 4. Our evaluation of the efficacy of our pipeline is uncompromised by the low  $\chi$  values because the distribution of SHARP values, the primary classification discriminant, is similar for both the artificial and real stars.

## 4.2. ARTDATA

Our second pipeline test used the ARTDATA package in IRAF to create a sample of synthetic starcount observations. We generated a catalogue of stars distributed according to a prescribed Galactic structure model (the interim model of Paper I), then added 700 extragalactic objects to the sample, with a power law distribution of  $N(A) \propto 10^{0.18*m}$ . This distribution is slightly shallower than galaxy distributions derived from deep  $R$  band galaxy count surveys (e.g., Crawford et al. 1999) and produces a fair level of contamination near the classification limit of the artificial data. Two types of galaxies were added - a de Vaucouleurs spheroid and an exponential disk - in a variety of orientations.

This catalogue was used to add objects to a set of synthetic  $BVRI$  images, generating realistic Poisson noise and adding a typical sky background. These “observations” were then evaluated through the photometry and classification pipeline.

Figure 8a shows the recovered fraction as a function of magnitude for the artificial data before object classification for all images in all passbands. The overall trend is similar to the ADDSTAR test. Figure 8b shows the recovered fraction of stars after classification. The recovered fraction

drops near the classification limit. Exploration of the data has shown this drop to be a result of the binning. Our methods retain 92% of the stars to the classification limit.

Figure 9 shows the magnitude- $\chi$  and magnitude-sharp distributions of the artificial galaxies measured in our data. 607 galaxies were photometered in at least two frames and 110 of those galaxies were above the classification limit. The classification parameters eliminated all but two of those galaxies - both faint de Vaucouleurs galaxies.

We evaluated the preselection parameters (sharpness and roundness) as classification tools by broadening the limits of DAOFIND. Changing the sharp limit added a handful of objects to the sample, while expanding the roundness limits (from -1:1 to -2:2) added 176 detections to the initial detection sample of the nearly 3000 objects. Visual inspection revealed the new detections to be mostly noise spikes and a few very bright stars. All but three bright stars among the new detections were rejected by the pipeline. From this, we conclude that the roundness and sharpness parameters of DAOFIND primarily separate out cosmic rays. The preselection parameters improperly remove less than 0.1% of the stars in observation and the stars removed are entirely bright saturated stars.

### 4.3. Deep ASA184 exposures

Our final test compared the two deep ASA184 exposures used for our search for the Sagittarius stream (Paper III) against overlapping Swope exposures initially intended to constrain halo asymmetry. We identified 430 objects observed in both the Swope and du Pont images that were brighter than the Swope-based classification limits for the two subfields. We then classified these objects using the finer resolution of the du Pont data. The distribution in magnitude- $\chi$  and magnitude-SHARP for the matched objects is shown in Figure 10. Of 36 galaxies photometered on both data sets, the pipeline correctly classified all of them on the Swope images. Of 394 stars in common, all but ten were correctly classified on the Swope images. Visual inspection revealed that the misclassified stars were near chip edges, bad columns or bright saturated stars. Figure 11 shows the recovered fraction as a function of magnitude relative to the classification limit of the Swope data. The recovered fraction of stars is 90-100% at this limit and the 50% level is reached at 0.9 magnitudes below the limit. This is similar to the results of the artificial star tests.

### 4.4. QSO Contamination

The classification methods discussed above are robust for galaxies that are morphologically distinct from stars. QSOs, however, are pointlike enough to be easily confused with stars. In Paper I, we noted that those objects can contribute over 25% of the blue “starcounts” at faint magnitudes.

QSO contamination is less of a problem in our study because these extragalactic objects are predominantly blue ( $B - V < 0.6$ ,  $R - I < 0.4$ ). Conveniently, the stars we study here are redder than this range (see §5.2). Nevertheless, some contamination may remain and the only way to mitigate the effect is to make a statistical correction to the counts.

To estimate just how much of a contribution QSOs will make to our starcounts, we estimated the number of these extragalactic objects that would fall into the faintest ( $20 < R < 21$ ), bluest ( $0.4 < R - I < 0.6$ ) region of the color-magnitude area from which photometric parallaxes are derived. Using the quasar luminosity function of Kron et al. (1991), convolved with the SDSS color distribution of the quasars listed in Richards et al. (2001), transformed from SDSS to standard filters using the transformations of Fukugita (1996), we estimate that this color-magnitude bin should have a contamination level of 32 galaxies per square degree.

Is this significant? This color-magnitude bin contains 150-500 stars per square degree, depending on Galactic latitude. This would mean that QSOs inflate the starcounts by 5-25%, with the starcount inflation greatest at high Galactic latitude. We repeated part of our analysis (§6) with the counts statistically corrected for compact galaxy contamination and found only a small effect on the derived density laws. We have thus chosen to leave this correction out of our analysis.

#### 4.5. Extragalactic Contamination - Overview

Considering the results of the tests of our pipeline, we are confident that we have photometered all stars to the stated imaging limits of each subfield, successfully stripped out nearly 100% of the galaxies from the starcounts to the classification limit and correctly classified 95-100% of the stars down to the classification limit.

Even more critical than the fraction of stars lost either through incompleteness or object classification are potential magnitude- or color-dependent biases induced. Our results show that the fraction of stars retained by the pipeline is a constant as a function of magnitude to the classification limit.

### 5. Photometric Parallax

There are many experiments that can be performed with a sample of starcount data. Our ultimate goal is to expand on the work in Paper I, generating a complex Galactic structure model and making comparisons between synthetic data generated by that model and real observed starcounts from our more extensive CCD data. In this article, we make a first evaluation of the density laws of the Milky Way stellar populations using a more simple method. We take a subsample of our data,  $RI$  photometry from seven of the Selected Areas, and use photometric parallax distance estimates of these stars to constrain the density laws of the thin disk, thick disk

and halo. The  $RI$  data were chosen because of the near uniformity of the data and the relative insensitivity to reddening of the  $RI$  passbands. Future contributions will exploit larger portions of the  $UBVRI$  data in an effort to constrain both the luminosity functions and spatial distributions of the Galactic stellar populations.

### 5.1. Dereddening

The photometry was dereddened using the high resolution COBE/DIRBE maps of Schlegel et al. (1998), which closely match the earlier work of Burstein & Heiles (1982). The reddening for the fields included in the photometric parallax study was generally small, with most of the fields near  $E_{B-V} \leq 0.05$  and only SA107 reddened by as much as  $E_{B-V} = 0.1$ . Some program fields not included in this analysis had higher values and SA95 showed evidence of differential reddening across the field. Interstellar reddening was corrected on a star-by-star basis by interpolating the Schlegel et al. maps at the position of each star and using the reddening coefficient for the Landolt  $UBVRI$  system derived in Schlegel et al.

The blue edge of the field photometry (see Figure 12) reflects the color of the main sequence turnoff stars at any particular magnitude. Previous studies (see, e.g., Unavane et al. 1996, C01) have shown the color of the blue edge as a function of magnitude to be remarkably consistent over a large range of  $(l, b)$ . It should thus serve as a reasonable landmark with which to check the derived reddening. Our subsequent study of the blue edge (Siegel et al., in preparation, hereafter Paper V) has revealed this blue edge color to align well in all of our program fields, which indicates we have made an accurate correction. The blue edge of SA95, a field which has patchy foreground reddening, was changed from an indistinct blur into a tight line after reddening correction (see Figure 12 and Paper V).

In the present analysis, we have assumed that dust obscuration is entirely in the foreground of our stars, which is inappropriate for the stars nearest the plane. Nevertheless, this assumption should be valid for the vast majority of stars because the scale height of the reddening layer is approximately 100 pc (Chen et al. 1999), which is far smaller than the distance of the bulk of the old disk, thick disk and halo stars we study. Even with a complex extinction model, the bulk of our stars would have nearly the full reddening correction applied.

### 5.2. The $M_R(R - I)$ Relation

The first step in determining photometric parallaxes is estimating the absolute magnitude of the program stars. We have derived a color-absolute magnitude relation in the  $RI$  passbands for dwarf stars and assumed *ab initio* that the bulk of our stars are faint dwarfs. The color-absolute magnitude relation utilizes parallaxes from the ESA Hipparcos catalogue of nearby dwarf stars and

corresponding photometry from Bessell (1990) and Leggett (1992).<sup>9</sup> The catalogue was cleaned of known binaries, stars with poor parallaxes ( $\sigma_\pi/\pi > 0.2$ ) and stars clearly removed from the trend of main sequence dwarf stars. After the application of the Lutz-Kelker (1973) correction, we fit a two-part relation of:

$$M_R = -6.862 + 61.375(R - I) - 108.875(R - I)^2 + 90.198(R - I)^3 - 27.468(R - I)^4 \quad 0.4 \leq R - I < 1.0 \quad (2)$$

$$M_R = -114.355 + 408.842(R - I) - 513.008(R - I)^2 + 286.537(R - I)^3 - 59.548(R - I)^4 \quad 1.0 \leq R - I < 1.5 \quad (3)$$

based on samples 230 and 195 stars, respectively. The fit is shown in Figure 13. These relations have a small discontinuity of approximately 0.1 magnitude at  $R - I = 1.0$ . The cutoff at  $R - I = 0.4$  eliminates potential uncertainties in the photometric parallax due to the main sequence turnoff as this is well-redward of the MSTO of even old populations.

The color-absolute magnitude relations have an uncertainty of 0.2-0.3 magnitudes. Therefore, the distance to any particular star has a moderate degree of error. If this scatter created corresponding *random* distance errors, it would be of small concern in a statistical analysis of 70,000 stars. However, the large absolute magnitude uncertainty plays a significant role in creating a *systematic* error in the distance estimates (Malmquist Bias) that will mask itself as a spatial trend. We now discuss Malmquist Bias and three other expected systematic biases – subgiant contamination, subdwarf bias and binarism – that must be accounted for.

### 5.3. Malmquist Bias Correction

In a conical magnitude-limited volume, the distance to which intrinsically bright stars are visible is larger than the distance to which intrinsically faint stars are visible. The effect of this is that brighter stars are statistically over-represented, and the derived absolute magnitude are too faint. This effect, known as Malmquist Bias (1920), was formalized into the general formula (shown here for our survey magnitudes and colors):

$$M(R) = M_0 - \frac{\sigma^2}{0.4343} \frac{d \log A(R)}{dR} \quad (4)$$

with the error in the magnitudes given as:

---

<sup>9</sup>Available online at <http://dep.physics.upenn.edu/~inr/cmd.html>

$$\sigma^2 = \frac{dM(R-I)^2}{d(R-I)} * \sigma_{R-I}^2 + \sigma_{M_R}^2 \quad (5)$$

where  $M_0$  is the absolute magnitude calculated for any star's  $R - I$  from the  $M_R = f(R - I)$  relation,  $A(R)$  is the differential counts evaluated at the apparent magnitude  $R$  of any star, and the errors correspond to the effect of photometric error propagated through the  $M_R = f(R - I)$  relation as well as the intrinsic astrophysical scatter in that relation, respectively.

A sophisticated computer model that produces artificial comparison data could be made to incorporate Malmquist bias naturally. Our simpler analysis in the distance-density domain requires a correction to the absolute magnitudes of the stars. It should be noted that this absolute magnitude correction is only applied in *statistical evaluations* of the stars. For any star considered as an individual object, this correction is inappropriate. When the stars are considered *en masse* however, each absolute magnitude must be corrected. This is analogous to the Lutz-Kelker correction applied to correct a  $\sigma_\pi/\pi$ -limited sample bias in our derivation of the color-absolute magnitude relationship and subdwarf bias (§5.2 and 5.5).

To make the Malmquist corrections, we produced a Hess diagram of each field, binned in 0.1 color intervals and 0.5 magnitude intervals. Faint magnitude bins were corrected to reflect the declining number of subfields complete to the corresponding depth. For each binned color range, the  $A(R)$  function was fit with a power series. The parameters of the fit change smoothly with color, which indicates a consistent fit to the color-magnitude-counts surface. For each star, the derivative for its color bin was evaluated at its magnitude and combined with the observational color error and the intrinsic scatter in the  $M_R = f(R - I)$  relation to derive the correction to its absolute magnitude.

The most distant stars in our sample are only marginally affected by Malmquist bias since the differential counts level out at faint magnitudes (as expected for an  $R^{-3}$  power law density distribution that approximates the Galactic halo). This causes the first derivative of the counts to be near zero, resulting in a minimal Malmquist correction. Nearby stars have a sharper gradient in differential counts, resulting in more substantial corrections.

#### 5.4. Subgiant Contamination

Our photometric parallax method assumes simplistically that every star in the data set is an unevolved dwarf star. While evolved giant and subgiant stars are fewer than main sequence stars by an order magnitude, giants and subgiants are much brighter than their main sequence brethren and can therefore be detected to greater distances and larger volumes. Subgiants could therefore contribute to the counts in a ratio much greater than predicted from the luminosity function.

Subgiant contamination was once speculated to be the source of the thick disk signal detected



by GR83 (Bahcall & Soneira 1984, in which the subgiants are referred to as “giants”). This argument has since been disproven (see Paper I), but the role of subgiant (and, for surveys at brighter apparent magnitudes, giant) contamination is a concern for any use of photometric parallaxes based on dwarf color-magnitude relations. The problem can be addressed on a statistical basis with an analytical correction.

At any particular color (and corresponding dwarf absolute magnitude  $M_D$ ) the dwarfs at any apparent magnitude  $m$  are at a distance  $r_D = 10^{(m-M_D+5)/5}$ . At this magnitude, the identically colored subgiants/giants of absolute magnitude  $M_{SG}$  are a distance  $r_{SG} = 10^{(m-M_{SG}+5)/5}$ . The number of giant contaminants,  $N_{SG}$  in the magnitude interval  $(m - \delta_m, m + \delta_m)$  and corresponding distance interval  $(r_{SG} - \delta_{r_{SG}}, r_{SG} + \delta_{r_{SG}})$  in solid angle  $\Omega$  can then be defined as:

$$N_{SG} = \Omega \kappa_{SG,D} \int_{r_{SG}-\delta_{r_{SG}}}^{r_{SG}+\delta_{r_{SG}}} \rho(r_{SG}) r_{SG}^2 dr_{SG} \quad (6)$$

where  $\kappa_{SG,D}$  is the intrinsic ratio of subgiants to dwarfs in a stellar population (as determined from the luminosity function) and  $\rho$  is the density of dwarfs as a function of distance. This is essentially the von Seeliger equation evaluated for a single spectral type. In the limit where the density law does is relatively constant over the distance interval  $\delta_{r_{SG}}$  and  $\delta_{r_{SG}} \ll r_{SG}$ , this can be rewritten as:

$$N_{SG} = \Omega \kappa_{SG,D} \rho(r_{SG}) \times 2r_{SG}^2 \delta_{r_{SG}} \quad (7)$$

The corresponding dwarf stars are evaluated in the same magnitude interval  $(m - \delta_m, m + \delta_m)$ . Our starcount analysis is directed at evaluating the number of dwarf stars in the distance interval  $(r_D - \delta_{r_D}, r_D + \delta_{r_D})$ . We therefore derive the density of dwarfs in this magnitude interval over the volume element  $V_D = 2\Omega r_D^2 \delta_{r_D}$ . The evolved stars contribute  $N_{SG}$  extra counts to this volume interval, producing a density inflation of:

$$\rho_{SG} = N_{SG}/V_D = \kappa_{SG,D} (r_{SG}^2 \delta_{r_{SG}}) \rho(r_{SG}) / (r_D^2 \delta_{r_D}) \quad (8)$$

For any color or dwarf absolute magnitude, we can explicitly define the subgiant distance  $r_{SG}$  in terms of the difference in absolute magnitudes between the dwarfs ( $M_D$ ) and subgiants ( $M_{SG}$ ) or the ratio of luminosities  $\frac{L_{SG}}{L_D}$ :

$$r_{SG} = r_D * 10^{(M_D - M_{SG})/5} = r_D * \sqrt{\frac{L_{SG}}{L_D}} \quad (9)$$

$$\delta_{r_{SG}} \sim \delta_{r_D} * \sqrt{\frac{L_{SG}}{L_D}} \quad (10)$$

Substituting equations 10 and 11 into equation 9 yields:

$$\rho_{SG} = \left(\frac{L_{SG}}{L_D}\right)^{1.5} \times \kappa_{SG,D} \times \rho \left(r_D * \sqrt{\frac{L_{SG}}{L_D}}\right) \quad (11)$$

At a constant  $\kappa_{SG,D}$  and  $\left(\frac{L_{SG}}{L_D}\right)$ , the gain in accessible subgiant detection volume due to greater subgiant luminosity is matched by the loss due to declining density if the density falls as  $r^{-3}$  or steeper. For most of our fields, the distance vector is close to the Galactic radial vector at large distances and the density should fall off as  $r^{-3}$  in an  $R^{-3}$  power law or de Vaucouleurs profile halo. SA107/SA184, however, are an exception. Because these two fields point into the Galaxy, models with spherical or near spherical halos will predict a *rise* in density between 5 and 10 kpc. Thus, evolved stars could be a more significant contaminant in those fields. The bias must be quantified and corrected if it is significant.

$\frac{L_{SG}}{L_D}$  and  $\kappa_{SG,D}$  are a function of color. For very red stars,  $\kappa_{SG,D}$  is low enough and  $\frac{L_{SG}}{L_D}$  high enough that evolved star contamination will be minimal. For late G-/early K-type stars, subgiant contamination might be more significant. We evaluated the effect on our density law derivation for our brightest bluest dwarf stars ( $5.8 \leq M_R < 6.8$ ). We determined  $\frac{L_{SG}}{L_D}$  and  $\kappa_{SG,D}$  with an  $[\text{Fe}/\text{H}]=-1.5$ , 16 Gyr isochrone from Bergbusch & Vandenberg (2001, hereafter BV01) for the distant halo and an  $[\text{Fe}/\text{H}]=-0.6$ , 12 Gyr isochrone to represent the nearby thick disk and old disk. The resultant values ( $\frac{L_{SG}}{L_D} \sim 26, \kappa_{SG,D} \sim .03$ ) were put into equation 11 to correct the predicted density for any particular model as a function of distance by:

$$\rho_{SG} = 4\rho(5r_D) \quad (12)$$

The total number of stars observed in a distance bin corresponding to a dwarf star apparent magnitude range of  $(m - \delta_m, m + \delta_m)$  is the sum of dwarfs and contaminating evolved stars:

$$\rho_{total} = \rho(D) + \rho(SG) \quad (13)$$

$$\rho_{total} = \rho(r_D) + 4\rho(5r_D) \quad (14)$$

This is a worst case scenario because the contamination levels drop off sharply for stars with fainter absolute magnitudes. We have found no significant effect of subgiants upon our analysis, even in SA184/SA107. The worst case scenario resulted in no significant change in the derived parameters of our best fit starcount models (§7) but improved the  $\chi^2$  of the fit from 2.7 to 2.2. The reason for this becomes obvious in light of the flattened halo models favored by our analysis in §7. Such models reduce the stellar density at the distance of potential subgiant contaminants compared with spherical halo models.

Our conclusion is that, even for our bluest and brightest main sequence stars, subgiant contamination has minimal impact on our density law derivation. We have therefore elected to

exclude this contribution from the density law derivation rather than attempt a more complex solution to account for the sharp slope of  $\frac{L_{SG}}{L_D}$  and  $\kappa_{SG,D}$  with absolute magnitude and color.

### 5.5. The Subdwarf Correction

The solar  $M_R = f(R - I)$  relation we define above is based on nearby metal-rich stars. However, this relation is systematically discrepant from the relation(s) for metal-weak stars due to the effect of line blanketing. Metal-rich stars are generally redder and fainter than their metal-weak, equal mass counterparts due to such effects. While the effect of line blanketing is small for G-type stars in the  $R$  passband, late-type K and M dwarfs develop strong molecular bands in the  $R$  passband with increased abundance, particularly from TiO and VO. The net result is that the main sequence of metal-poor stars is blueward of the solar-metallicity sequence. If photometric parallaxes are derived from stellar colors, the distance to metal-poor stars will thus be systematically overestimated. Because the mean abundance of stars changes with spatial position, ignoring the metallicity effects in the derivation of photometric parallax results in systematic errors for the derived spatial structure.

Deriving a metal-poor  $M_R = f(R - I)$  relation is problematical since few metal-poor stars have both precise trigonometric parallaxes and high-quality  $RI$  photometry. We have adopted a strategy similar to that of Gizis & Reid (1999). The relation given in §5.2 is for local stars that have an average metallicity of approximately  $[\text{Fe}/\text{H}]=-0.2$ . We have defined a second relation for the metal poor “sd” stars of Gizis (1997), which have an average estimated mean  $[\text{Fe}/\text{H}]$  of -1.2. The relation for these stars, with Lutz-Kelker correction, is:

$$M_R = 2.03 + 10.0 \times (R - I) - 2.21 \times (R - I)^2 \quad (15)$$

We find that this quadratic equation is consistent with the two-part linear calibration of Gizis & Reid (1999) and consistent with the bright subdwarf tail of theoretical isochrones from BV01 (see Figure 14). For a star of given metallicity and color, its absolute magnitude can be estimated by linear interpolation between the two derived ridgelines and linear extrapolation beyond the metal-poor ridgeline.<sup>10</sup>

Following GR83, we assign metallicities to stars based on their location in the Galaxy, using an empirical metallicity distribution. We assume that derived mean metallicities for tracer stars (e.g., K giants) apply to the dwarf population and modify the vertical abundance gradient of Yoss et. al. (1987) to:

---

<sup>10</sup>Although the  $[\text{Fe}/\text{H}]=-2.0$  stars form an apparent sequence fainter than the  $[\text{Fe}/\text{H}]=-1.2$  ridgeline, we have elected not to establish a third ridgeline. Our reasons are that the uncertainties in the  $[\text{Fe}/\text{H}]=-2.0$  subdwarfs are large, there are no  $[\text{Fe}/\text{H}]=-2.0$  stars bluer than  $R - I = 0.75$  with which to extend the sequence, and we have truncated the metallicity gradient so that no star is assumed to be more metal-poor than  $[\text{Fe}/\text{H}]=-1.5$ .

$$\begin{aligned}
 0 < z < 0.7kpc & \quad [Fe/H] = -0.4 \times z \\
 0.7 < z < 7.5kpc & \quad [Fe/H] = -0.28 - 0.18 * (z - 0.7kpc) \\
 7.5kpc < z & \quad [Fe/H] = -1.5
 \end{aligned}
 \tag{16}$$

where  $z$  is in units of kpc. The first two abundance gradients are directly from Yoss. But, unlike Yoss et al., we truncate the gradient at the point it reaches  $[Fe/H] = -1.5$ , a likely average metallicity value of the halo (Carney et al. 1996).

A similar empirical abundance gradient is derived by Trefzger et al. (1995). This model does not account for any radial variation in metallicity. The existence of such a radial gradient in the field stars of any population beyond the thin disk has yet to be demonstrated (see, e.g., Rong et al. 2001). While vertical metallicity gradients have been refuted for the halo (Searle & Zinn, 1978; Carney et al. 1990) and are debatable for the thick disk (see, e.g., Rong et al. 2001; cf. Gilmore et al. 1995, R96), such analyses have attempted to isolate each population and assess their abundance distributions independently. This is a risky venture because of the difficulty in separating overlapping stellar populations and because apparent metallicity gradients may be the product of transitions from monometallic regions dominated by metal-rich populations to monometallic regions dominated by metal-poor populations. However, one can make a comparison between our modified abundance gradient and one produced by a favored model abundance distribution. Adopting the density laws derived in §7 and assuming traditional average abundances of  $[Fe/H]=0.0, -0.6$  and  $-1.5$  for the thin thick, thick disk and halo, respectively, we find the Yoss gradient is slightly ( $\sim 0.1 - 0.2$  dex) too metal-rich at Galactic heights dominated by the thick disk (2-6 kpc). A slope of 0.21 dex/kpc in the second relation produces a better match to the model abundance gradient but the difference in photometric parallaxes is negligible. Given the similarity in results, we opt for simplicity and retain the empirical abundance gradient, which also has the advantage of avoiding a priori assumptions concerning population mixture ratios.

With each star, a preliminary distance is determined using the near-solar metallicity relation. We then derive a metallicity based upon the star’s height above the plane and linearly interpolate from the two color-magnitude relations to derive a corrected absolute magnitude. This process is performed iteratively until the distance converges to within 5 parsecs. The effect of this correction upon the derived density laws is a subtle steepening of the density gradient for stars at large heights above the Galactic midplane.

We note that systematic errors in our subdwarf correction would result in systematic errors in our derived density laws. For example, systematically underestimating the abundance of distant stars would cause us to underestimate the absolute magnitudes and underestimate the distance, resulting in steeper density gradients and reduced scale heights. Such concerns are addressed more fully in §8.

We summarize in Figure 15 the effects of galaxy separation, subdwarf correction and

Malmquist bias corrections upon the density distribution in SA101, one of our deepest program fields. The affects of bias correction upon the density profile are subtle and primarily at the extreme ends of the data.

## 5.6. Binarism

It is well established that a substantial fraction of the Population I stars in the Milky Way are not single stars but are in binary pairs, with estimates for the binary fraction ranging from 50% in G-type stars (see, e.g., Duquennoy & Mayor 1991) to 30-35% in K- and M-dwarfs (Fischer & Marcy 1992; Reid & Gizis 1997). Even a binary with an extraordinarily large separation (500 AU) will be enclosed within a 1" seeing disk at distances greater than 500 pc and thus will be imaged as a single star. The effect of unresolved binaries upon our analysis is not intuitive. Binaries manifest two observational effects: The increased apparent luminosity of the "star" and the shift in apparent color. The former will cause the distance to the "star" to be underestimated while the effect of the latter will vary depending on the relative brightness and temperature of the two stars.

To examine the effects of binarism upon our survey, we have simulated a density analysis that includes the effect of binaries. We adopted the  $M_R = f(R - I)$  relation of equations 2 and 3 and generated a sample of "stars" with colors chosen from that relation perturbed by Gaussian dispersion in  $R - I$  and  $M_R$  and a density distribution matching a set density law (a 300 parsec exponential for simplicity). For a fraction of the stars, we added a companion chosen either at random from the luminosity function or specified to be nearly equal in mass to the primary. The color and magnitude of each primary star was then reset to the combined characteristics of the binary. We then evaluated the density distribution of the stars using the original  $M_R = f(R - I)$  calibration and the inferred density law was compared with the input value.

Figure 16 shows the effect of binaries upon the inferred density law for the following binary star fractions: (a) 50% fraction of binaries, with equal numbers of equal-mass and random binaries, (b) 50% fraction of binaries, all random, (c) 25% fraction of binaries, all equal-mass, (d) 25% fraction of binaries, all random. The net effect of ignoring binaries is to steepen the derived density law compared to the true density law. If we assume a binary fraction of 50%, then the *inferred* scale height in a photometric parallax evaluation is approximately 80% of the *actual* value. The small difference between simulations with equal-mass and random binaries show that the actual composition of the binaries has only a small impact on this evaluation.

One should use caution, however, in applying this correction, as there is some controversy on the binary fraction of halo and thick disk stars and whether this binary fraction changes with spectral type (see discussion in Majewski 1992, §5.3; Fischer & Marcy 1992; Reid & Gizis 1997). For simplicity, our analysis proceeded without this correction. However, our final results list both uncorrected values, which are effectively lower limits, and values corrected for a 50% binary

fraction.

## 6. Analysis Methods

### 6.1. The Assumed Density Law Forms

We have used a family of standard density laws to describe the populations of the Milky Way. A more thorough analysis of this subject can be found in Paper I. We summarize that discussion here.

Disk structures are usually parameterized in cylindrical coordinates by separable radial and vertical exponentials,

$$\rho(z, r) = \rho_0 e^{\frac{-z}{Z_0}} e^{\frac{-r}{R_0}} \quad (17)$$

where  $z$  is the distance from the midplane,  $r$  is the planar distance from the Galactic Center, and  $Z_0$  and  $R_0$  are the scale height and length respectively. The coefficient  $\rho_0$  is the normalizing factor, calibrated to produce the observed local stellar density of the disk population.

Exponentials have the benefit of being easily fit in distance-log(density) space where they form straight lines. The slope and y-intercept yield scale height and normalization respectively. A similar form uses the  $sech^2$  function to parameterize the vertical distribution.

$$\rho(z, r) = \rho_0 sech^2\left(\frac{-z}{2Z_0}\right) e^{\frac{-r}{R_0}} \quad (18)$$

This functional form has three advantages. First, it avoids a singularity at  $z = 0$ . Second, it has a more firm theoretical basis in that stars in an isothermal sheet should have such a distribution (Camm 1950, 1952; van der Kruit & Searle 1981). Finally, at large distances, the  $sech^2$  function approximates the observed exponential density profile.

Starcounts have retained the exponential formalism almost exclusively despite the fact that surface brightness studies of edge-on galaxies have been using  $sech^2$  formalism for nearly two decades. While a switch to  $sech^2$  seems physically justified, there is growing evidence that the midplane luminosity of edge-on galaxies *is* sharply peaked (de Grijs et al. 1997) and exponential functions may indeed provide more reasonable midplane fits than once thought. In addition, Hammersley et al. (1999) have shown that an exponential distribution, despite the singularity problems, is a much better fit to the infrared starcounts of our own galaxy (although Gould et al. 1996 show the opposite result in optical starcounts). Given the reasonable observational evidence on both sides, we have chosen to try both vertical distribution functions although the differences should be relatively minor in our program.

Spheroid population density laws come in numerous formulations. The most common is the de Vaucouleurs (1948) spheroid used to describe the surface brightness profile of elliptical galaxies. This law has been deprojected into three dimensions via the Young (1976) formulation as:

$$\rho(R_g) = \rho_0 \exp[-7.669(R_g/R_e)^{1/4}] / (R_g/R_e)^{0.875} \quad (19)$$

where  $R_e$  is the effective radius or half-light radius and  $R_g$  is the Galactocentric distance in spherical coordinates. This formulation is valid as long as  $\frac{R_g}{R_e} > 0.2$  which is true in all our fields for  $R_e < 30$  kpc. Other models have used the power law formulation:

$$\rho(R_g) = \rho_0 \frac{1}{a_0^n + R_g^n} \quad (20)$$

where  $a_0$  is the core radius (an often omitted parameter). The power law formalism, beside being a convenient fitting form, is similar to the distribution predicted by cold dark matter (CDM) simulations (see, e.g., Navarro et al. 1997). The CDM formalism is, however, slightly more complex. An adaptation to this context is:

$$\rho(R_g) = \frac{\rho_0}{(R_g/R_s)(1+R_g/R_s)^2}$$

where  $R_s$  is the scale radius. This differs from the straight power law formalism in that the slope of the density law will be shallower in the inner regions of the spheroid than the outer regions. It should be noted, however, that the stellar halo and dark matter halo are not necessarily the same structure. The dark halo must have a shallower density law ( $R^{-2}$ ) and larger mass than the stellar halo to account for the kinematics of the halo. Thus, formalisms based on CDM simulations are of questionable value for starcounts.

In spheroid formalisms,  $R_g$  is not true galactocentric radius. It is corrected for the axial ratio  $\frac{c}{a}$  as  $R_g^2 = \sqrt{r^2 + (\frac{z}{(c/a)})^2}$ .

For our analysis, the formal distribution of the bulge spheroid is unimportant. We lack the low-latitude first and fourth quadrant fields required to apply constraints to the bulge spheroid and have therefore adopted a distribution from the literature of a simple spherical  $R_g^{-3}$  power law normalized to .02% of the solar neighborhood density. We have left those parameters fixed in all fits.

The more important spheroidal component in our analysis is the halo. The choice of halo density law is somewhat arbitrary since the difference between the de Vaucouleurs law and power law are subtle when seen through such a roughly ground lens as starcounts (although N97 claim that the de Vaucouleurs distribution underpredicts the faint counts to a noticeable degree). We have elected to explore models that use both prescriptions.

The thick disk and halo density normalizations are given in comparison to the density of the thin disk at the Sun. This definition of normalization is slightly confused in the literature with some sources normalized to the percentage of *total* stars in the Solar neighborhood that belong to that population, while others normalize to the *ratio* of thick disk or halo stars to thin disk stars. In this contribution, we shall use the latter definition although the difference is only important at high normalizations.

The normalization to the solar neighborhood naturally must account for the Sun’s location away from the Galactic center and slightly above the Galactic midplane. We have taken the values for solar radius and height to be 8.0 kpc (Reid 1993) and 15 pc (Yamagata & Yoshii, 1992; N97), respectively. The latter value is consistent with the determination of Humphreys & Larsen (1995) if the thin disk has a low (250-300 pc) scale height and this value also corresponds to minima in our  $\chi^2$  fitting of the population models.

## 6.2. Searching Parameter Space

The use of photometric parallaxes allows us to make a direct evaluation of the spatial density law. Rather than try to fit the structure of the Galaxy in the observed parameter space of colors and magnitudes, we translate the observations to discrete density measurements at various points in the Galaxy. This allows us to reduce measurement of the density distribution to the comparatively simple process of fitting the distance-density distribution simultaneously along our seven lines of site. In so doing, we are essentially fitting the density distribution over the two-dimensional Galactic  $r - z$  surface. In our case, we assume azimuthal symmetry although we could generalize the formalism to account for triaxiality. The goodness of fit parameter is straightforward - a  $\chi^2$  value of the predicted trend in density-distance space against the actual data.

Finding the  $\chi^2$  minimum proved problematical. The standard grid-search and gradient algorithms became trapped in local minima. After many attempts with more elegant methods, we elected to take a straight-forward approach to finding the best density law: Generating millions of density distribution combinations with variations of the population parameters over a wide grid of possible values. Each model was compared to all seven fields simultaneously and a total seven-field  $\chi^2$  was calculated. The resultant  $\chi^2$  values were then examined to find minima. A first pass was made with a broad range of values at coarse resolution. Broad minima were found and further investigations used increasingly finer resolution and decreasing range. To render the problem computationally feasible, subsequent passes varied several key parameters while others were held fixed. Parameters were rotated in and out of variation until convergence to a minimum.



### 6.3. Binning the Sample

A concern in our approach is that the von Seeliger equation is a convolution of the density distribution and luminosity function, which are unlikely to be independent of each other. The luminosity function can vary with location in the Galaxy (and population) and the density distribution can vary depending on spectral type. For example, younger stars tend to be more confined than older stars in their vertical distribution from the Galactic midplane. Thus, the problem is not simply two-dimensional (i.e., distance against density) but *three-dimensional* (i.e., distance against density against luminosity).

Sophisticated models incorporate this convolution effect in their simulations (see, e.g., Robin & Creze 1986; Paper I). An alternative strategy is to break the data into groups of similar stars. Ideally, one might evaluate stars of identical *mass*. However, because deriving masses for stars is even more subject to systematic errors and requires additional degrees of extrapolation, we have elected to evaluate stars of identical estimated absolute magnitudes. Our analysis is limited to the range of magnitudes  $5.8 \leq M_R \leq 10.2$ . For solar metallicity stars, this corresponds to approximately  $6.3 \leq M_V \leq 12$  or spectral types K0 to M4.

### 6.4. Convergence and Parameter Drift

We found that our exploration of parameter space defined likelihood minima quite easily for the two disk populations. The parameters of the halo, however, diverged quickly to edge of parameter space. With the power law halo, this was manifested as a derivation of low power law indices, low axial ratios and high normalizations ( $\sim 1.0$ , 0.3 and 0.6% respectively). The de Vaucouleurs halo also diverged to low axial ratios, high effective radii and high normalizations ( $\sim 0.3$ , 10 kpc and 0.5% respectively). With the halo parameter drift came a commensurate secondary effect of flatter thin and thick disks of low scale heights (150 and 500 pc respectively).

It is, of course, possible that those results are the correct description of the Galaxy. Our analysis was designed specifically to ignore *a priori* assumptions about the populations and find the model that best fits the data, regardless of how it compared with previous results. However, the derived parameters are so at variance with the prior literature that one is led to believe that a fundamental flaw is present in the method.

The likely explanation for this divergence is the general insensitivity of starcounts to halo parameters, a problem magnified by the crudity of our analysis of photometric parallaxes. It is also possible that the halo has a more complex field to field variation than the simple models parameterized above. Our survey would be among the first starcount surveys to be complete enough and deep enough to encounter problems of halo substructure affecting an analysis of starcounts. An underconstrained complex halo density distribution could easily be divergent in such an analysis. The case for a complex halo is made in detail in §8.

## 7. Best Fit Conventional Models

### 7.1. Disk Models With Constrained Halos

Given the failure of any of our models with an unconstrained halo to converge, we decided to adopt fixed halo distributions from the existing literature. We then allowed the thick and thin disk parameters to vary freely (except for the thin disk scale height in the intrinsically brightest stars, which are undersampled close to the sun) to see which provided the best description of the Galaxy.

Models for the halo population were taken from L96, N97, B99 (which is similar to the Paper I halo) and R00 (the flattened version of which is identical to the halo derived in C01). The results are listed in Table 3. The spherical halos adopted by N97 and B99 produce dramatically poorer fits than flattened halo models. This is illustrated in Figure 17, which compares the interim model of Paper I against the isodensity points for our brightest ( $5.8 \leq M_R < 6.8$ ) stars along our seven lines of sight. These stars provide the greatest leverage on the halo because they probe the farthest into the Galaxy. We can immediately discern that the interim model is a good description of the density distribution at the SGP and a reasonable, but imperfect description of the density law outside of  $R_g=5$  kpc. On the other hand, there are significant density overpredictions toward the Galactic Center in the distant bins of SA107/SA184. These overpredictions are also seen in the less-flattened Besançon model to a lesser but still noticeable degree.

The best halo prescription appears to be either the L96 flattened de Vaucouleurs spheroid or the Besançon/C01 flattened power law. In fact, the predictions of the two models are similar. Both produce a low scale height, high normalization thick disk. Table 4 lists the best fit to all four absolute magnitude data bins given the Besançon halo formulation and exponential disks and Table 5 gives the best fit using *sech*<sup>2</sup> disks. Note that the values in Tables 3-5 are not corrected for binarism. The errors bars are taken at the point at which  $\chi^2 = \min(\chi^2)+1$ . The asymmetry in the disk scale length error bars is caused by the ease with which sharp density gradients can be ruled out in comparison to shallow gradients. The  $\chi^2$  interval of 2.5-3.0 encapsulates any power law halo with an axial ratio of 0.5-0.7 and a power law index of 2.5-3.5, with low index, low axial ratio halos favored. The thick disk that results from any of those halo prescriptions has the general parameters of  $Z_o = 700-900$  pc,  $R_0 = 3000-5000$  pc,  $\rho = 6-10\%$ . It is curious that the lowest absolute magnitude bin has a significantly higher thin disk scale height. This could reflect either that scaleheight increases at fainter magnitudes or, possibly, that binary fraction declines at fainter magnitudes.

Figures 18 and 19 show the overplot of the observed isodensity points on the model isodensity contours for our “best-fit” models. While those two models are a reasonable description of the Galaxy, especially for nearby stars, there remain systematic discrepancies for the most distant density contours. In particular, the models overpredict the density toward the Galactic Center and underpredict the density in the outer halo regions. The systematic, as opposed to random, nature

of the over- and underpredictions, indicates that the standard models are still in need of revision.

## 7.2. The Shape of the Galaxy

Table 6 lists the revised parameters of our new model. The parameters are a general synthesis of the magnitude-differentiated descriptions listed in Tables 3-5 and reflect the range of values occupying the  $\chi^2 = 2.5 - 3.0$  region of parameter space. The listed parameters primarily pertain to the bluer stars and do not reflect the increased thin disk scale height at faint absolute magnitudes. Both raw values (i.e, uncorrected for binarism) and corrected values (with a binary fraction of 50%) are listed.

An old disk with an exponential scale height lower than the canonical value (325 pc) has been indicated in much of the recent literature, with the exception of C01. We have only parameterized the thin disk with a single old population, which may be too simplistic (for example, N97 uses three fixed disks). Our data near the Galactic midplane are too sparse to constrain more than one thin disk component. In addition, at the faint absolute magnitudes that our study explores, the thin disk is dominated by the old disk component (see Paper I). The equivalent  $sech^2$  scale height places the Galaxy at the somewhat thin end of the spectrum of spatial parameters of edge-on galaxies (de Grijs 1998).

Our thin disk scale length of 2.25 kpc is shorter than the 3-4 kpc canonical value, but the error bars enclose the longer estimates of R96, L96 and B99. A short thin disk scale length is also indicated by infrared starcounts (see, e.g., Ruphy et al. 1996; Drimmel & Spergel 2001). Studies of edge-on disk galaxies have found the average  $\frac{R_0}{Z_0}$ , in which  $Z_0$  is defined slightly differently as the scale height in the density formulation  $\rho(z) = sech^2 \frac{z}{Z_0}$ , to be approximately  $5.9 \pm 0.4$  (de Grijs & van der Kruit 1996). The axial ratio is dependent on Hubble type (de Grijs, 1998) and “super-thin” galaxies with axial ratios as high as 14 have been found (Matthews 2000). The Galaxy’s axial ratio of  $\sim 4$  places it among the Sc galaxies.

Our derived thick disk scale height is similar to the C01 result and comparable to the Besançon results (R96), albeit with a noticeably higher normalization than the latter. Comparing normalizations between different studies is difficult because some authors are unclear exactly *to what* their thick disk and halo are being normalized. It is possible that since both our study and C01 normalize to the old disk alone, we overestimate the normalization by ignoring contributions from younger populations that have a smaller signature in our study. Based on the three-disk normalizations used in N97, a better normalization for our thick disk might be 4-6%.

The high thick disk scale heights of Paper I, GR83 and other studies are likely the result of surveying a single direction of sky near a Galactic pole and adopting a fixed near-spherical halo. It was concern about halo flattening and degeneracy that motivated this study – to determine if non-polar fields demanded a more complex density distribution. Such concerns appear to have been justified. While a 1.5 kpc height, 2% normalization thick disk is a suitable fit to SA141, as

attested by Figure 17, the non-polar fields argue strongly for a much more substantial thick disk population.

Presumably, the spatial distribution of the field stars is a reflection of their dynamics. Any self-consistent dynamical Galaxy model should simultaneously account for both. The measured  $\sigma_W$  of the thick disk is approximately  $40 \text{ km s}^{-1}$  (Norris 1986; Sandage 1987; Sandage & Fouts 1987; Carney et al. 1989; Beers & Sommer-Larsen, 1995; Guo 1995; Reid et al. 1995; Ojha et al. 1996; Chiba & Beers 2000), which implies a vertical scale height of around 1 kpc, with possibly as much as 10% of the local stars included in this high  $\sigma_W$  population (Sandage & Fouts 1987; Sandage 1987; Casertano et al. 1990; Reid et al. 1995) although Guo (1995) argues for a lower normalization of 3%. While the thick disk scale height implied by these studies is roughly compatible with our results, it is also roughly compatible with just about every measure of thick disk scale height that has been made (see Table 1). A fraction of local stars in the high  $\sigma_W$  population as high as 10% would be compatible with our own results and those of R96 and C01. Finally, Majewski (1992) and Guo (1995) have argued that thick disk kinematics dominate out to at least  $Z = 4.5 - 5.5$  kpc. In our model, the thick disk dominates the density distribution to a similar height above the plane.

Our thick disk scale length is compatible with previous starcounts results as well as the kinematical estimate of Chiba & Beers (2000). More important than the precise value of the thick disk scale length, however, is that the thick disk scale length is longer than the thin disk scale length, at least when evaluated in our brightest absolute magnitude bin – which has the smallest uncertainty. Although it has been standard practice in the literature to assume that the two lengths should be equal or comparable, in many starcounts studies, including this one, the error bars on the scale lengths are too large for firm conclusions to be drawn. L96 is a notable exception, showing a thick disk scale length longer than the thin disk at a  $5\sigma$  level of significance. In addition, studies of edge-on disk galaxies have shown that some of them (especially early-type galaxies) exhibit radial variations in scale height, indicative of thick disks with scale lengths longer than the thin disks (see, e.g., de Grijs & Peletier 1997).

## 8. Toward More Complex Density Distributions

There could be a number of reasons why we are unable to fit a standard density law to the halo starcounts and why even the best models from the literature have systematic problems. These divide into two categories: Problems with our analysis and problems with the density law itself.

Our analysis could be compromised by a poor subdwarf correction. This would produce systematic effects. While our simplified metallicity correction fit the data on subdwarf parallaxes reasonably well, the number of stars with good parallaxes and good photometry is small and the scatter large. There is a critical need for high precision parallaxes and broadband photometry of metal-poor stars, a situation that could be remedied by ground-based photometry and the

astrometric space missions of the next decade. Figure 14, however, shows that while the subdwarf correction is large for the latest stars, it is small for the early K dwarfs that provide our only probe into the halo. Unless the subdwarf correction is grossly incorrect, this would not produce the effects we are seeing.

Moreover, the apparently small subdwarf correction in blue stars may itself asymptote at low abundances so that even significantly poorer halo populations would have similar absolute magnitudes to  $[\text{Fe}/\text{H}]=-1.5$  stars. This “guillotine effect”, in which the metallicity correction asymptotes as metallicity declines, has been known at least since first defined in the context of ultraviolet excesses by Sandage (1969). We do not have nearly enough subdwarfs with parallaxes to characterize this effect and the scatter of the red  $[\text{Fe}/\text{H}]=-2.0$  stars in Figure 14 cautions against attempting to define such an effect. Nevertheless, the possibility of a guillotine effect – especially in the bright blue stars upon which our analysis leans heavily – mitigates to some extent the danger of subdwarf correction errors for very low metallicity populations in the Galactic halo.

Related to the subdwarf problem is the possibility of an incorrect metallicity gradient. The Yoss et al. metallicity gradient is poorly constrained in the halo. While it is generally agreed that  $[\text{Fe}/\text{H}]\sim-1.5$  is a characteristic halo metallicity, the halo has a high metallicity dispersion and may, in fact, have some metallicity substructure (Carney et al. 1996; King 1997). In addition, none of our models have incorporated a *radial* metallicity gradient but only a vertical variation. This could be too simplistic, although a radial gradient of increasing metallicity toward the Galactic Center would cause systematic biases producing the opposite effect of the observed density overpredictions. Moreover, radial metallicity gradients have only been demonstrated for the thin disk (Rong et al. 2001), a population that is minimally represented in our most distant stars. Metallicity scatter or substructure would presumably not induce first order systematic effects.

A final source of error could be an overzealous galaxy separation effort. The broadening of the stellar  $\chi$  and SHARP loci at faint magnitudes could cause faint stars to be preferentially misclassified. Such a problem, however, would result in a *uniform overprediction* of density at faint magnitudes, not the selective over- and underprediction that is observed to occur.

The second possibility is that the density formulations we have used, while reasonable descriptions for the local Galaxy, are too simple to describe the Galactic density distributions at great distances from the Sun. There are several density law modifications that could resolve the observed problems:

1. *Thick Disk Flaring.* Our models have assumed that the thick disk scale height is constant with radius from the Galactic center. This formulation has only been tested in the Galactic context to rather short distances and primarily toward the Galactic anti-center. It is possible that the thick disk is flared, with a scale height that *increases* with radius. This would help eliminate some of the density overprediction in SA107/SA184.

The remaining five fields in our survey cover a small dynamic range in planar distance. When we evaluate these five fields independently of SA107/SA184, the resultant uncorrected thick disk

scale height is  $\sim 0.8\text{-}1.2$  kpc, although this value is highly dependent upon the adopted halo model. This suggests that the local thick disk scale height may indeed be larger than the scale height in the inner Galaxy. Alternatively, this result could indicate that the radial density distribution of the thick disk is not exponential, as we have assumed. A thick disk that is exponential locally but that has a shallower radial density gradient in the inner Galaxy would also fix the inner Galaxy isodensity contours.

2. *Triaxiality.* Larsen & Humphreys (1996) have argued for a triaxial halo based upon asymmetries found in halo starcounts from APS-POSS. Our data cannot detect this proposed distribution because we do not have fields in the lower-latitude areas noted to have asymmetry by Larsen & Humphreys. This would also leave unexplained the overpredictions of the model in the SA107/SA184 fields, which would show minimal effects from the Larsen & Humphreys asymmetry given the location of these two fields near the Galactic meridian and would show opposite effects (i.e., overprediction in one, underprediction in the other) if they were affected by a halo asymmetry.

3. *A Complex Halo.* Evidence has been growing for some time that simple descriptions of the Galactic halo are inadequate. Studies of the outer halo through either giant stars or bright halo stars have derived a spherical  $R^{-3}$  distribution (Paper I; N97; Majewski et al. 2000; Morrison et al. 2000; Majewski et al. 2002). Studies of fairly nearby main sequence stars (Larsen & Humphreys 1994; R96; L96; R00; C01) and microlenses (see, e.g., Samurovic et al. 1999) have derived a flattened halo distribution. Some surveys have found a single axial ratio too restrictive and have adopted a  $\frac{c}{a}$  ratio that increases with Galactocentric radius to explain the spatial distribution of RR Lyrae/HB stars (Hartwick 1987; Preston et al. 1991; Kinman et al. 1994; Layden 1993; Layden 1995; Wetterer & McGraw 1996; Sluis & Arnold 1998), globular clusters (Zinn 1993) and main sequence stars (Gilmore et al. 1985).

Studies of the kinematics and abundance of both field stars and globular clusters show that the halo is better described as having *two* subpopulations – a flattened inner subpopulation with a metallicity gradient and slow-rotation kinematics and a round outer subpopulation with no metallicity gradient and anisotropic kinematics (Zinn 1993; Dinescu et al. 1999). Recent studies of halo field stars selected either by proper motion (Carney et al. 1996) or metallicity (Sommer-Larsen & Zhen 1990; Allen et al. 1991; Chiba & Beers 2000) have presented a similar picture – a flattened inner halo – and a round  $R^{-3}$  component that lacks a metallicity gradient. Additional support for dual halo models can be drawn from the apparent dichotomy in detailed chemical abundances of halo stars (Nissen & Schuster 1997).

Starcounts studies have never explored this possibility. Such models might resolve many of the disagreements in starcounts results. In a dual halo model, nearby stars (R96; L96; C01) are dominated by the flattened inner halo while distant stars (Paper I; N97) are dominated by the spherical outer halo.

Adopting a two halo formalism, however, leads to a poor solution. If the  $R^{-3.5}$  spherical power

law for the outer halo is extrapolated into SA107/SA184, the result is a severe overprediction in the counts. This can be mitigated by expanding the core radius of the the outer halo power law or lowering the power law index. That change, however, results in a density gradient in our high-latitude fields that is far shallower than the observed gradient. We have thus far been unable to find a uniform model that correctly predicts all of the fields, although there are several avenues that show promise for future work.

In particular, in an effort to fit all of the density contours, we attempted three variations of the standard halo that showed some improvement over conventional models. Our first used a power law in which the power law index increases with radius. This was motivated by the results of recent hierarchical clustering models of galaxy formation, which indicate that the power law indices of accreted dark matter halos should fall toward the inner regions, producing a shallow  $R^{-1.5}$  inner halo density gradient and a steep outer  $R^{-3}$  to  $R^{-4}$  outer halo density gradient (see, e.g., Dubinski & Carlberg 1991; Navarro et al. 1997; Subramian et al. 2000; Davé et al. 2001). While the metal-poor stellar halo discussed here is a completely separate entity from the (presumably) primordial dark-matter halo, the density law of the former should, after all, follow the gravitational potential of the latter. If that were the case, distant field stars of the stellar halo could offer a means of testing dark-matter models. Our second variation used confocal ellipsoids to describe the halo. This projection produces elliptical inner isopleths and round outer isopleths. Our final model attempted to use the  $\frac{c}{a} = f(R)$  formulation of Preston et al. (1991) to account for axial ratio changes. All three halo formulations produce measurable improvements to the *initial* fits but do not converge, which may once again reflect the general insensitivity of starcounts to halo parameters – an insensitivity that is only worsened when more free parameters are added.

On the other hand, it is possible that while a dual halo description of the Galaxy is qualitatively accurate, the very nature of the model renders it unamenable to conventional quantitative analysis. The spherical outer halo *may not have a smooth density distribution* but be comprised of overlapping streams of stars. Substructure and/or breaks in the halo density profile have been directly observed in giant stars (Majewski et al. 2002), main-sequence stars (Majewski et al. 1994, 1996; Newberg et al. 2001; Dinescu et al. 2002) and BHB/RR Lyrae halo stars (Yanny et al. 2000; Ivezić et al. 2000; Vivas et al. 2001). These studies have suggested that at large Galactocentric radii, the halo may be largely or *entirely* comprised of overlapping streams and that smooth density distribution may only apply to the inner Galaxy.

It is unclear if a substructured outer halo could resolve the remaining problems in our model. The deviations from our model appear to be *systematic*, rather than the *random* deviations one would see if looking out through a “can of worms”. Additionally, Johnston (1998) has indicated that even major accretion events might be undetectable in starcounts studies. If the filling factor of the star streams is high enough, what appears as a “can of worms” in the finely tuned studies of bright tracer stars could be blurred into a vague, indistinct, seemingly uniform population in starcount studies. Moreover, because we have only seven fields in our program, our ability to distinguish between systematic and random effects in the outer halo is limited.

If a flared thick disk were incorporated to reconcile the overpredictions of SA107/SA184, however, halo substructure could explain the underpredictions in our other fields, particularly SA141, which appears to be in the direction of an outer halo stream of Newberg et al. (although the stream appears to be at larger distances than we are sensitive to). Thus, the idea of a dual halo in which the outer halo is not a uniform structure but a vague ensemble of star streams, remains an intriguing possibility and a likely resolution of the outstanding discrepancies in our model.

## 9. Implications for Galactic Formation

Starcounths are, of course, a means to an end. The actual numerical values of the various parameters of the populations are less scientifically important than what they tell us about the Galaxy in general – for example, the origin of the various components.

A number of scenarios have been proposed for the origin of the thick disk (see review in Majewski 1993). It is clear from its main sequence turnoff color that the thick disk includes few, if any, main-sequence stars younger than a few Gyrs. At present, a popular formation mechanism is that the thick disk formed by tidal heating of the early Galactic thin disk either by merging galaxies (see, e.g. Quinn et al. 1993, hereafter Q93; Walker et al. 1996; Huang & Carlberg 1997; Sellwood et al. 1998) or the late infall of stellar clumps formed during the dissipational collapse of the Galaxy (Noguchi 1998). In tidal heating or merger scenarios, the Galactic gas content would be kinematically heated by the event but would eventually cool off and settle down to form the present thin disk. Because stars are effectively collisionless particles, however, they would retain the dynamical heat of the event.

Alternatively, the thick disk may have formed in a dissipative collapse following the rapid formation of the halo and ending in the formation of the thin disk (see, e.g. Larson 1976; Jones & Wyse 1983). Majewski (1993) outlined evidence to support a variant scenario in which the thick disk represented the initial structure formed in the Galaxy via a global collapse as first theorized by Eggen, Lynden-Bell & Sandage (1962, hereafter ELS), and this was followed by the formation of the halo by accretion of small stellar systems (see also Sandage 1990).

Evidence in favor of a heating origin for the thick disk comes from studies of chemical abundances (Nissen & Schuster 1991; Fuhrmann 1998; Gratton et al. 2000; Prochaska et al. 2000) and kinematics (Carney et al. 1989; Beers & Sommer-Larsen 1995; Ojha et al. 1996), which seem to show a continuum of properties from nearby halo to thick disk and then a discontinuity between the thick disk and thin disk. One must always temper claims for such discontinuities with the possibility of selection bias. Thick disk stars are often selected for kinematical study by their chemical properties or for chemical study by their kinematics. In a late-heating scenario, the most extreme kinematical and most extreme chemical portions of the thick disk could be the same. The more complete samples of globular clusters (Zinn 1993) and field stars (Majewski 1992,



1995; Chen 1997; Chen 1999; Chiba & Beers 2000) show kinematical gradients in the disks and a kinematical break between thick disk and halo. In addition, the time of such a violent heating event can be constrained to be between the age of the thick and thin disk stars. It therefore must have occurred fairly early in the Galaxy’s history since the oldest stars of the thin disk are between 8 and 12 Gyr in age (Janes & Phelps 1994; Bergeron et al. 1997; Leggett et al. 1998; Jiminez et al. 1998; Wood & Oswalt 1998; Knox et al. 1999; Carraro et al. 1999; Montgomery et al. 1999; Liu & Chaboyer 2000). The thick disk stars are generally thought to be older than this (Gilmore & Wyse 1987; Carney et al. 1989; Rose & Agostinho 1991; Gilmore et al. 1995). One important caveat, however, is that the differences in ages (generally around 1-2 Gyr) are small compared to the uncertainties. Given the difficulty in measuring the age of field stars, the age difference between the thin and thick disk is still debatable.

In our opinion, the most compelling recent evidence for a merger origin is that the star formation history gleaned from abundance patterns does not conform to expectations from dissipational formation (Prochaska et al. 2000), although this evidence comes with the caveat that the Prochaska et al. thick disk stars do not have a large abundance overlap with the thin disk stars to which they are being compared. There is also strong support from the extragalactic angle in that thick disks are not seen in all edge-on disk galaxies (van der Kruit & Searle 1981; Morrison, Boroson & Harding 1994; Morrison et al. 1997; Fry et al. 1999), which suggests a more stochastic process is at work.

The origin of the halo is thought to be either through the rapid global collapse of the protogalactic gas cloud (ELS) or the accretion of protogalactic fragments (Searle & Zinn 1978). The accretion hypothesis is in line with favored cold dark matter cosmologies, which predict a hierarchical galaxy formation process (see, e.g., White & Rees 1978; Navarro et al. 1997). §8 recounts the evidence on both sides of the halo formation question and notes the attempts to reconcile the observational evidence by dividing the halo into two distinct populations.

Four Galactic populations (old disk, thick disk, inner halo and outer halo) can account for most of the properties of Galactic field stars found in the literature. The outer halo – as described by Zinn (1993) and Chiba & Beers (2000), described as just “the halo” by Majewski (1993) and completely absent from studies of comparatively nearby main sequence stars (e.g., R96, L96, R00) – is more or less spherical, shows phase-space substructure, is chemically inhomogenous and disjoint from the inner halo. It is the product of Galactic accretion of globular clusters and dwarf galaxies. The inner halo – as described by Zinn (1993) and Chiba & Beers (2000), difficult to distinguish from the thick disk in the Galactic poles and therefore blurred with the thick disk into “IPII” by Majewski (1992, 1993, 1995) and Paper I, described as “the halo” in R96, L96, R00 and C01 – is flattened, has kinematical and metallicity gradients and is chemically and kinematically overlapped with the thick disk. It is likely the product of an ELS-like collapse (Sandage 1990). The thick disk is then the compact, chemically and kinematically homogenous structure described in R96 and C01 and Prochaska et al. – possibly formed by a merger early in the Galaxy’s history.

Such hybrid models for the formation of the halo have been proposed (see, e.g., Sandage 1990; Majewski 1993; Norris 1994; Chiba & Beers 2000). The principal contribution of starcounts in constraining Galactic formation scenarios lies in revealing the underlying shape, chemistry and ages of the stellar population through sophisticated modeling, study of detailed stellar color distributions or ultraviolet excesses – all of which we plan to pursue with our present data set. Our study of photometric parallaxes, however, provide some support for the hybrid formation model in that we show discrepancies between the relatively simple canonical density laws and the observed density distribution of Galactic field stars. These discrepancies could be resolved by invoking structural properties unique to the hybrid model. For example, the density overprediction in the inner Galaxy would be explained by thick disk flaring, which Q93 assert would be characteristic of a kinematically heated thick disk. Additionally, the density underpredictions in the outer Galaxy would be resolved by a second spherical substructured halo – a population characteristic of an accreted halo.

The general picture that is emerging in the study of the Galaxy is one in which both global collapse and accretion have probably played significant roles in producing the extant stellar populations. Accretion may be manifested in two modes – the subsuming of accreted stellar populations into the outer halo and the tidal inflation of the early thin disk by a particularly large merger. Global collapse would be manifested in the inner halo. Continued exploration of our own data set and that of SDSS will continue to improve our understanding.

## 10. Conclusions

Our photometric parallax survey of seven Kapteyn Selected Areas has produced a number of intriguing results:

- The thin disk is well described by a double exponential of raw scale height 280 pc and scale length 2-2.5 kpc. Its axial ratio is consistent with the ratios observed in edge-on Sc galaxies. The faintest stars in the sample show some evidence of an elevated scale height (350 pc). Interestingly, recent results indicate that the scale height of thin disk white dwarfs may also be much higher than the canonical thin disk scale height (Majewski & Siegel 2002; Nelson et al. 2002). However, if the binary fraction declines for faint stars, this would produce a similar effect.
- The thick disk is well described by a double exponential of raw scale height 700-1000 pc and scale length 3-4 kpc. Approximately 6-10% of the local old stars are part of the thick disk. There is some evidence that the disk is flared, which is consistent with a kinematic heating origin for the thick disk.
- If the binary fraction of Population II stars is 50%, the scale heights of the thin and thick disk for blue stars would increase to 350 and 900-1200 pc, respectively. The elevated thin disk scale height of the faintest stars is 440 pc.

- Fits to the halo density law do not converge in our simulations. Flattened ( $\frac{c}{a} \sim 0.6$ ) power law ( $\rho \propto R_{gc}^{-2.5}$ ) halos are generally favored.

- Some of the remaining discrepancies between our model and the data could be resolved by a dual halo model in which the inner halo is flattened and the outer halo is a roughly spherical “can of worms”, consisting of distinct overlapping streams of stars. Such a dual halo would also reconcile many of the discrepancies in the literature into a single model.

- Evidence for a flared thick disk and a dual halo would support the notion that the Milky Way has grown at least in part through the accretion of external systems.

Future contributions from this series will explore the new CCD starcount data in greater detail with the goal of strengthening our understanding of Galactic stellar populations and the underlying chemodynamical history that they reflect.

This research was supported by NSF grants AST-9412265 award to IBT and SRM, grant AST-9412463 awarded to INR, CAREER Award AST-9702521 to SRM, the David and Lucille Packard Foundation (SRM, MHS) and the Observatories of the Carnegie Institute of Washington (SRM, INR, IBT). The authors thank Robert Link and Jamie Ostheimer for helpful discussions and the numerous Swope telescope operators for their assistance.

## REFERENCES

- Allen, C., Poveda, A., & Schuster, W. J. 1991, *A&A*, 244, 280
- Baade, W. 1944, *ApJ*, 100, 137
- Bahcall, J. N. & Soneira, R. M. 1980, *ApJS*, 44, 73
- Bahcall, J. N. & Soneira, R. M. 1984, *ApJS*, 55, 67
- Beers, T. C. & Sommer-Larsen, J. 1995, *ApJS*, 96, 175
- Beichman, C. A., Chester, T. J., Skrutskie, M., Low, F. J., & Gillett, F. 1998, *PASP*, 110, 480
- Bergbusch, P. A. & Vandenberg, D. A. 2001, *ApJ*, *astro-ph/0102480* [BV01]
- Bergeron, P., Ruiz, M. T., & Leggett, S. K. 1997, *ApJS*, 108, 339
- Bessell, M. S., 1990, *A&AS*, 83, 357
- Burstein, D. & Heiles, C. 1982, *AJ*, 87, 1165
- Buser, R., Rong, J. & Karalli, S. 1998, *A&A*, 331, 934
- Buser, R., Rong, J. & Karalli, S. 1999, *A&A*, 348, 98 [B99]
- Camm, G. L., 1950, *MNRAS*, 110, 305
- Camm, G. L., 1952, *MNRAS*, 112, 155

- Carney, B. W., Latham, D. W., & Laird, J. B. 1989, *AJ*, 97, 423
- Carney, B. W., Aguilar, L., Latham, D. W., & Laird, J. B. 1990, *AJ*, 99, 201
- Carney, B. W., Laird, J. B., Latham, D. W., & Aguilar, L. A. 1996, *AJ*, 112, 668
- Casertano, S., Ratnatunga, K. U. & Bahcall, J. 1990, *ApJ*, 357, 435
- Carraro, G., Girardi, L., & Chiosi, C. 1999, *MNRAS*, 309, 430
- Chen, B. 1997, *ApJ*, 491, 181
- Chen, B. 1999, *A&A*, 344, 494
- Chen, B., Figueras, F., Torra, J., Jordi, C. Luri, X. & Galadí-Enríquez, D. 1999, *A&A*, 352, 459
- Chen, B. et al. 2001, *ApJ*, 553, 184 [C01]
- Chiba, M. & Beers, T. C. 2000, *AJ*, 119, 2843
- Crawford, S. M., Majewski, S. R. & Bershady, M. A., 1999, *BAAS*, 195, 136.06
- Davé, R., Spergel, D. N., Steinhardt, P. J., & Wandelt, B. D. 2001, *ApJ*, 547, 574
- de Grijs, R. & Peletier, R. F. 1997, *A&A*, 320, L21
- de Grijs, R., Peletier, R. F. & van der Kruit, P. C. 1997, *A&A*, 327, 966
- de Grijs, R. & van der Kruit, P. C. 1996, *A&AS*, 117, 19
- de Grijs, R. 1998, *MNRAS*, 299, 595
- del Rio, G. & Fenkart, R. 1987, *A&AS*, 68, 397 [DF87]
- de Vaucouleurs, G. 1948, *Annales d’Astrophysique*, 11, 247
- Dinescu, D. I., Girard, T. M., & van Altena, W. F. 1999, *AJ*, 117, 1792
- Dinescu, D. I., Majewski, S. R., Girard, T. M., Méndez, R. A., Sandage, A. R., Siegel, M. H., Kunkel, W. E., Subasavage, J. P. & Ostheimer, J. C. 2002, *ApJ in press*
- Drimmel, R. & Spergel, D. N. 2001, *ApJ*, 556, 181
- Dubinski, J. & Carlberg, R. G. 1991, *ApJ*, 378, 496
- Duquenois, A. & Mayor, M. 1991, *A&A*, 248, 485
- Eggen, O. J., Lynden-Bell, D., & Sandage, A. R. 1962, *ApJ*, 136, 748 [ELS]
- Fenkart, R., Topaktas, L., Boydag, S., & Kandemir, G. 1987, *A&AS*, 67, 245
- Fischer, D. A. & Marcy, G. W. 1992, *ApJ*, 396, 178
- Fry, A. M., Morrison, H. L., Hardin, P. & Boroson, T. A., 1999, *AJ*, 118, 1209
- Fuhrmann, K. 1998, *A&A*, 338, 161
- Fukugita, M., 1996, *AJ*, 111, 1748
- Gilmore, G. & Reid, I. 1983, *MNRAS*, 202, 1025 (GR83)
- Gilmore, G. 1984, *MNRAS*, 207, 223

- Gilmore, G., Reid, N., & Hewett, P. 1985, MNRAS, 213, 257
- Gilmore, G. & Wyse, R. F. G. 1987, NATO ASIC Proc. 207: The Galaxy, 247
- Gilmore, G., Wyse, R. F. G., & Jones, J. B. 1995, AJ, 109, 1095
- Gizis, J. E. 1997, AJ, 113, 806
- Gizis, J. E. & Reid, I. N. 1999, AJ, 117, 508
- Gould, A., Bahcall, J. N., & Flynn, C. 1996, ApJ, 465, 759
- Gratton, R. G., Carretta, E., Matteucci, F. & Sneden, C. 2000, A&A, 358, 671
- Guo, X., 1995, *Galactic Structure, Kinematics and Chemical Abundance from UBV Photometry and Absolute Proper Motions to B about 22.5 Towards the South Galactic Pole*, Ph.D. Thesis, Yale University
- Hammersley, P. L., Cohen, M., Garzón, F., Mahoney, T. & López-Corredoira, M. 1999, MNRAS, 308, 333
- Harris, W. E., Fitzgerald, M. P. & Reed, B. C. 1981, PASP, 93, 507
- Hartwick, F. D. A. 1987, in *The Galaxy*, ed. G. Gilmore & B. Carswell, NATO ASIC Proc. 207, (Dordrecht: Reidel), p. 281
- Huang, S. & Carlberg, R. G. 1997, ApJ, 480, 503
- Humphreys, R. M. & Larsen, J. A. 1995, AJ, 110, 2183
- Ivezić, Z. et al. 2000, AJ, 120, 963
- Janes, K. A. & Phelps, R. L. 1994, AJ, 108, 1773
- Jimenez, R., Flynn, C., & Kotoneva, E. 1998, MNRAS, 299, 515
- Johnston, K. V. 1998, ApJ, 495, 297
- Jones, B. J. T. & Wyse, R. F. G. 1983, A&A, 120, 165
- King, J. R. 1997, AJ, 113, 2302
- Kinman, T. D., Suntzeff, N. B., & Kraft, R. P. 1994, AJ, 108, 1722
- Knox, R. A., Hawkins, M. R. S., & Hambly, N. C. 1999, MNRAS, 306, 736
- Kron, R. G., Bershad, M. A., Munn, J. A., Smetanka, J. J., Majewski, S. & Koo, D. C. 1991, in *The Space Distribution of Quasars*, ed. Crampton, D., ASP Conf. Ser. Vol 21, (San Francisco: ASP), p. 32
- Kuijken, K. & Gilmore, G. 1989, MNRAS, 239, 605
- Landolt, A. U. 1992, AJ, 104, 340
- Larsen, J. A. & Humphreys, R. M. 1994, ApJ, 436, L149
- Larsen, J. A. & Humphreys, R. M. 1996, ApJ, 468, L99
- Larsen, J. A., 1996, *The Shape of the Galaxy*, PhD Thesis, University of Minnesota [L96]

- Larson, R. B. 1976, MNRAS, 176, 31
- Layden, A. C. 1993, PASP, 105, 1367
- Layden, A. C. 1995, AJ, 110, 2288
- Leggett, S. K., 1992, ApJS, 82, 351
- Leggett, S. K., Ruiz, M. T., & Bergeron, P. 1998, ApJ, 497, 294
- Liu, W. M. & Chaboyer, B. 2000, ApJ, 544, 818
- Lutz, T. E. & Kelker, D. H. 1973, PASP, 85, 573
- Malmquist, G. 1920, Lund Medd., Ser. 2, No. 22
- Majewski, S. R. 1992, ApJS, 78, 87
- Majewski, S. R. 1993, ARA&A, 31, 575
- Majewski, S. R., Munn, J. A., & Hawley, S. L. 1994, ApJ, 427, L37
- Majewski, S. R., 1995, in The Formation of the Milky Way, eds. Alfaro, E. J. & Delgado, A. J. (Cambridge: Cambridge University Press), p. 199
- Majewski, S. R., Munn, J. A., & Hawley, S. L. 1996, ApJ, 459, L73.
- Majewski, S. R. 1999, in Tenth Canary Islands Winter School of Astrophysics: Globular Clusters, eds. C. Martínez Roger, I. Pérez Fournon & F. Sánchez (Cambridge: Cambridge Univ. Press), p.43
- Majewski, S. R., Siegel, M. H., Kunkel, W. E., Reid, I. N., Johnston, K. V., Thompson, I. B., Landolt, A. U., & Palma, C. 1999, AJ, 118, 1709 [Paper III]
- Majewski, S. R., Ostheimer, J. C., Kunkel, W. E., & Patterson, R. J. 2000, AJ, 120, 2550
- Majewski, S. R. & Siegel, M. H. 2002, ApJ, *in press*
- Majewski, S. R., Ostheimer, J.C., Kunkel, W. E., Patterson, R. J., Johnston, K. V., Crane, J. D., Helio, R. P., Rhee, J., Siegel, M. H., Palma, C. & Hummels, C. 2002, *in preparation*
- Matthews, L. D. 2000, AJ, 120, 1764
- Méndez, R. A. & Guzman, R. 1998, A&A, 333, 106
- Monet, D. G., et al., 1996, USNO-SA2.0, (Washington: US Naval Obs.)
- Montgomery, M. H., Klumpe, E. W., Winget, D. E., & Wood, M. A. 1999, ApJ, 525, 482
- Morrison, H. L., Boroson, T. A., & Harding, P. 1994, AJ, 108, 1191
- Morrison, H. L., Miller, E. D., Harding, P., Stinebring, D. R., & Boroson, T. A. 1997, AJ, 113, 2061
- Morrison, H. L., Mateo, M., Olszewski, E. W., Harding, P., Dohm-Palmer, R. C., Freeman, K. C., Norris, J. E. & Morita, M. 2000, AJ, 119, 2254
- Navarro, J. F., Frenk, C. S., & White, S. D. M. 1997, ApJ, 490, 493

- Nelson, C. A., Cook, K. H., Axelrod, T. S., Mould, J. R., Alcock, C., ApJ, *in press*
- Newberg, H. J., et al. 2002, *in press*
- Nissen, P. E. & Schuster, W. J. 1991, A&A, 251, 457
- Nissen, P. E. & Schuster, W. J. 1997, A&A, 326, 751.
- Noguchi, M. 1998, Nature, 392, 253
- Norris, J. 1986, ApJS, 61, 667
- Norris, J. E. 1994, ApJ, 431, 645
- Ng, Y. K., Bertelli, G., Chiosi, C. & Bressan, A. 1997, A&A, 324, 65 [N97]
- O’Connell, D. J. K. 1958, Ricerche Astronomiche, Specola Vaticana, Proceedings of a Conference at Vatican Observatory, Castel Gandolfo, May 20-28, 1957, Amsterdam: North-Holland, and New York: Interscience, 1958, edited by O’Connell, D.J.K.
- Ojha, D. K., Bienaymé, O., Robin, A. C., Crezè, M., & Mohan, V. 1996, A&A, 311, 456
- Ojha, D. K., Bienaymé, O., Mohan, V. and Robin, A. C. 1999, A&A, 351, 945
- Phleps, S., Meisenheimer, K., Fuchs, B. & Wolf, C. 2000, A&A, 356, 108
- Preston, G. W., Shectman, S. A., & Beers, T. C. 1991, ApJ, 375, 121
- Prochaska, J. X., Naumov, S. O., Carney, B. W., McWilliam, A., & Wolfe, A. M. 2000, AJ, 120, 2513
- Quinn, P. J., Hernquist, L., & Fullagar, D. P. 1993, ApJ, 403, 74 [Q93]
- Reid, M. J. 1993, ARA&A, 31, 345
- Reid, I. N. & Gizis, J. E. 1997, AJ, 113, 2246
- Reid, I. N. & Majewski, S. R. 1993, ApJ, 409, 635 [Paper I]
- Reid, I. N., Hawley, S. L., & Gizis, J. E. 1995, AJ, 110, 1838
- Reid, I. N., Yan, L., Majewski, S., Thompson, I. & Smail, I. 1996, AJ, 112, 147 [Paper II]
- Reid, I. N., Majewski, S. R., Siegel, M. H., & Thompson, I. 1998, in Galactic Halos: A UC Santa Cruz Workshop, ed. D. Zaritsky, ASP Conf. Ser. 136, 3
- Richards, G. T. et al. 2001, AJ, 121, 2308
- Robin, A. & Crézé, M. 1986, A&A, 157, 71
- Robin, A. C., Haywood, M., Crézé, M., Ojha, D. K. & Bienaymé, O. 1996, A&A, 305, 125 [R96]
- Robin, A. C., Reylé, C. & Crézé, M. 2000, A&A, 359, 103 [R00]
- Rong, J., Buser, R., & Karalli, S. 2001, A&A, 365, 431
- Ruphy, S., Robin, A. C., Epchtein, N., Copet, E., Bertin, E., Fouque, P. & Guglielmo, F. 1996, A&A, 313, L21
- Rose, J. A. & Agostinho, R. 1991, AJ, 101, 950

- Samurović, S., Ćirković, M. M., & Milosević-Zdjelar, V. 1999, MNRAS, 309, 63
- Sandage, A. 1969, ApJ, 158, 1115
- Sandage, A. & Fouts, G. 1987, AJ, 93, 592
- Sandage, A. 1987, AJ, 93, 610
- Sandage, A. 1990, JRASC, 84, 70
- Schlegel, D. J., Finkbeiner, D. P. & Davis, M. 1998, ApJ, 1998, 500, 525
- Searle, L. & Zinn, R. 1978, ApJ, 225, 357
- Sellwood, J. A., Nelson, R. W., & Tremaine, S. 1998, ApJ, 506, 590
- Siegel, M. H., Majewski, S. R., Reid, I. N. & Thompson, I. B. 2002, *in preparation* [Paper V]
- Sluis, A. P. N. & Arnold, R. A. 1998, MNRAS, 297, 732
- Sommer-Larsen, J. & Zhen, C. 1990, MNRAS, 242, 10
- Stetson, P. B. 1987, PASP, 99, 191
- Subramanian, K., Cen, R., & Ostriker, J. P. 2000, ApJ, 538, 528
- Trefzger, Ch. F., Pel, J.W. & Gabi, S. 1995, A&A, 304, 381
- Tritton, K. P. & Morton, D. C. 1984, MNRAS, 209, 429
- Unavane, M., Wyse, R. F. G., & Gilmore, G. 1996, MNRAS, 278, 727
- van der Kruit, P. C. & Searle, L. 1981, A&A, 95, 105
- Vivas, A. K. et al. 2001, ApJ, 554, L33
- von Hippel, T. & Bothun, G. D. 1993, ApJ, 407, 115
- von Seeliger, H. 1898, Abh. K. Bayer. Akad. Wiss., Ser. II, KI. 19, 564
- Walker, I. R., Mihos, J. C., & Hernquist, L. 1996, ApJ, 460, 121
- Wetterer, C. J. & McGraw, J. T. 1996, AJ, 112, 1046
- White, S. D. M. & Rees, M. J. 1978, MNRAS, 183, 341
- Wood, M. A. & Oswalt, T. D. 1998, ApJ, 497, 870
- Wyse, R. F. G. & Gilmore, G. 1989, Comments on Astrophysics, 13, 135
- Yamagata, T. and Yoshii, Y. 1992, AJ, 103, 117
- Yanny, B. et al. 2000, ApJ, 540, 825
- Yoshii, Y. 1982, PASJ, 34, 365
- Yoshii, Y., Ishida, K., & Stobie, R. S. 1987, AJ, 92, 323.
- Yoss, K. M., Neese, C. L. & Hartkopf, W. I. 1987, AJ, 94, 1600.
- Young, P. J., 1976, AJ, 81, 807



Zinn, R. 1993, in *The Globular Cluster-Galaxy Connection*, ed. G. H. Smith & J. P. Brodie, ASP Conf. Ser. Vol. 48, 38

### Figure Captions

Fig. 1.— Previous measures of the thick disk (IPII) exponential density law normalizations (abscissa) and scale heights (ordinate). This plot does not include Chen et al. 2001, which is displaced significantly off of the figure. The dotted lines reflect the percentage of the Galactic stellar mass residing in the thick disk for various combinations of parameters. Squares points represent the results of previous photometric parallax surveys.

Fig. 2.— Our starcount fields in Aitoff projection. The darkened squares are those analyzed in this contribution. Fields represented as open squares have been reduced through the data pipeline but lacked complete  $RI$  data for this particular study. Later analyses will examine all twelve fields.

Fig. 3.— The magnitude difference of standard stars measured in our pipeline compared with the photometry of Landolt (1992). The smaller error bars correspond to the Tek 5 data. The apparent trend in  $B$  is not statistically significant.

Fig. 4.— The magnitude-SHARP and magnitude- $\chi$  distributions of a typical field, in this example the  $V$  band frame of the central field of SA107. The upper loci in each panel are non-stellar objects while the main locus near SHARP=0.0,  $\chi$ =1.0 are stars. The horizontal lines indicate the cuts applied to those fields while the vertical lines show the classification limit of the field. More stringent  $\chi$  limits were found occasionally to filter out bright stars, such as the clump of stars with elevated  $\chi$  values around  $V = 17$  show in the figure. SHARP is therefore adopted as the primary discriminant in our program.

Fig. 5.— The recovered fraction of stars added to a diverse sample of CCD images with respect to the classification limit. Panel (a) shows the overall trend, while panel (b) highlights the region near the classification limit.

Fig. 6.— The recovered fraction of stars with respect to the classification limit after galaxy decontamination. Panel (a) shows the overall trend, while panel (b) highlights the transition zone.

Fig. 7.— The magnitude-SHARP and magnitude- $\chi$  distribution of artificial stars. This can be contrasted to the distribution of real data seen in Figure 4. Note the decreased  $\chi$  values for bright stars and the much tighter clumping of the stellar locus. This is the result of unrealistically excellent photometry for artificial stars.

Fig. 8.— The recovered fraction with respect to the classification limit of stars added to the CCD frames with ARTDATA. (a) shows the recovered fraction before object classification, (b) the recovered fraction after.

Fig. 9.— The magnitude-SHARP and magnitude- $\chi$  distribution of ARTDATA artificial galaxies photometered by DAOPHOT. This can be compared with the distribution of real data seen in Figure 4.

Fig. 10.— The magnitude- $\chi$  and magnitude-SHARP distribution of objects photometered in two Swope fields and deeper du Pont imaging. Open boxes are galaxies measured on both telescopes, filled circles are stars measured on both telescopes, dots are stars measured in only one dataset. These classifications are based on the du Pont imaging. Lines represent the cuts made in magnitude, SHARP and  $\chi$  for classification on the 1 meter data. The field ASA184-3 had a brighter classification limit and has been shifted 0.6 magnitudes to align the classification limits. Note the upward slope of the stellar locus where the 2.5 meter data become saturated.

Fig. 11.— The recovered fraction of stars in relation to the classification limit of the Swope images from a comparison of Swope data to deeper du Pont imaging.

Fig. 12.— An illustration of the blue edge of the field stars and the reddening correction. Panel (a) shows the blue edge of the field SA107, a field where it is clearly defined. The arrows delineate the MSTO of the thick disk and halo, respectively (see Paper V). Panel (b) shows the underreddened field SA95, which has highly differential reddening. Panel (c) shows the blue edge of SA95 after reddening correction and demonstrates the much tighter blue edge that results. Note the superiority of the SA107 data (which was primarily obtained with the Tek 5 chip) to that of SA95 (entirely Tek 3) in both depth and scatter.

Fig. 13.— The absolute magnitude-color distribution of stars in the HIPPARCOS catalogue used to calibrate photometric parallaxes. The solid line shows our fit to the data, excluding potential binaries (the second brighter sequence) and subdwarf stars (marked with error bars). Note the MSTO of the old Galactic populations, which is well blueward of the  $R - I = 0.4$  cutoff we use in our evaluation of the density laws.

Fig. 14.— Our adopted subdwarf correction. The solid line reflects the H-R diagram shape we derive at near solar metallicity and the dashed line shows the H-R diagram we derived for  $[\text{Fe}/\text{H}] = -1.2$ . The H-R curves derived in Gizis & Reid (1999) for both subdwarfs (“sd”,  $[\text{Fe}/\text{H}] \sim -1.2$ ) and extreme subdwarfs (“esd”,  $[\text{Fe}/\text{H}] \sim -2.0$ ) are shown as dot-dash lines. Also included is a fit to the upper main sequence of an  $[\text{Fe}/\text{H}] = -1.14$  isochrone from BV01 (long dash line), which truncates near the top of the main sequence. The points are metal-poor stars with trigonometric parallax taken from Gizis (1997) after application of the Lutz-Kelker correction.

Fig. 15.— The effect of Malmquist and subdwarf bias correction and galaxy decontamination on the density distribution of stars in SA101. Note that while removing extragalactic objects substantially changes the density profile, the Malmquist and subdwarf bias corrections are subtle. The Malmquist bias correction shifts the density profile at small distances while the subdwarf correction shortens the distance range.

Fig. 16.— An evaluation of the effect of binaries upon the derived density law for different ratio of near-equal mass and random mass binaries. The panels show the actual density law (solid line) against the derived density law (dotted line) for various binary fraction. Note that for each sample, the result is a steepening of the measured density law and consequent underestimation of the scale height.

Fig. 17.— Comparison of the density isopleths in our bluest stars (symbols) along the seven lines of sight used in this study (solid lines) against the predictions from the Paper I model (dashed lines). Note the reasonable fit to the SGP but the strong overpredictions toward the Galactic Center. Units of density are stars per  $\text{pc}^{-3}$ . Crosses, asterisks, diamonds, triangles, squares and x's are, respectively, densities of -3.0, -4.0, -4.5, -5.0, -5.5, and -6.0 stars per  $\text{pc}^{-3}$ .

Fig. 18.— Comparison of the density isopleths in our bluest stars along the seven lines of sight used in this study (solid lines) against the predictions from the model parameterized in Table III using the R00 II halo (dashed lines). Units are identical to figure 17. Note the excellent fit to nearby points but the overpredictions toward the Galactic center and underpredictions in the outer Galaxy.

Fig. 19.— Comparison of the density isopleths in our bluest stars along the seven lines of sight used in this study (solid lines) against the predictions from the model parameterized in Table III using the L96 halo (dashed lines). Units are identical to figure 17. Note the excellent fit to nearby points but the overpredictions toward the Galactic center and underpredictions in the outer Galaxy. Note also that the minor difference between this figure and figure 19.

Table 1. Previous Starcount Results

$Z_{0,thin}$ (pc)	$R_{0,thin}$ (kpc)	$\rho_{thick}$	$Z_{0,thick}$ (kpc)	$R_{0,thick}$ (kpc)	$\rho_{halo}$	$R_{e,halo}$ (kpc)	$\frac{c}{a}$	Reference
310-325	...	.0125-.025	1.92-2.39	...	...	...	...	Yoshii 1982 <sup>a</sup>
300	...	.02	1.45	...	.002	3000	0.85	GR83
325	...	.02	1.3	...	.002	3000	0.85	Gilmore 1984
280	...	.0028	1.9	...	.0012	...	...	Tritton & Morton 1984
200-475	...	.016	1.18-2.21	...	.0016	...	0.8	Robin & Creze 1986
300	...	.02	1.0	...	.001	...	0.85	del Rio & Fenkart 1987
285	...	.015	1.3-15	...	.002	2360	flat	Fenkart et al. 1987
325	...	.0224	.95	...	.001	2.9	0.9	Yoshii et al. 1987
249	...	.041	1.0	...	.002	3000	0.85	Kuijken & Gilmore 1989
350	3.8	.019	.9	3.8	.0011	2.7	0.84	Yamagata & Yoshii 1992
290	...	...	0.86	...	...	4.0	...	von Hippel & Bothun 1992
325	...	.0225	1.5	...	.0015	3.5	0.80	Paper I
325	3.2	.019	0.98	4.3	.0024	3.3	0.48	L96
...	2.5	.056	0.76	2.8	.0015	2.44-2.75 <sup>b</sup>	0.6-0.85	R96, R00
290	4.0	.059	0.91	3.0	.0005	2.69	0.84	Buser et al. 1998, B99
240	2.5	.061	.79	2.8	...	...	0.6-0.85	Ojha et al. 1999
330	2.250	.065-.13	0.58-0.75	3.5	.00125	...	0.55	Chen et al. 2001

<sup>a</sup>The stars Yoshii 1982 assigned to the halo have been here assigned to the thick disk.

<sup>b</sup>Power Law Index replacing  $R_e$ .

Table 2. Program Fields

Selected Area	$(\alpha, \delta)_{1950.0}$	$(l, b)$
141	01:05.4,-29:34	245,-86
118	02:17.4,-14:36	186,-66
95	03:52.6,+00:09	189,-38
96	04:50.6,+00:05	198,-26
194-18	05:09.5,+07:37	194,-18
101	09:54.6,-00:14	239,+40
102	10:51.0,-0:49	253,+50
104	12:40.6,-00:16	299,+62
107	15:36.6,-00:10	6,+41
184	20:52.4,-44:39	356,-40
90	22:14.4,+15:25	77,-33
114	22:39.6,+00:26	70,-48

Table 3. Halo Model Comparisons to Intrinsically Bright ( $5.8 \leq R - I < 6.8$ ) Stars

$\rho_{thin}$ ( $pc^{-3}$ )	$Z_{thin}$ ( $pc$ )	$R_{thin}$ ( $pc$ )	$\rho_{thick}$ ( $\rho_{thin}^{-1}$ )	$Z_{0,thick}$ ( $pc$ )	$R_{0,thick}$ ( $pc$ )	$\rho_{halo}$ ( $\rho_{thin}^{-1}$ )	$\chi^2$
		Exponential Disks, L96 halo ( $\frac{c}{a} = 0.48, R_e = 3.28$ kpc)					
$0.0048 \pm .0012$	280	$2200^{+14000}_{-800}$	$0.080 \pm .020$	$710 \pm 60$	$3800^{+4800}_{-1000}$	$.0024 \pm .0010$	2.61
		Exponential Disks, R00 halo I ( $\frac{c}{a} = .76, n = 2.44$ )					
$0.0047 \pm .0012$	280	$2000 \pm ^{+7400}_{-700}$	$0.081 \pm .017$	$770 \pm 60$	$4000 \pm ^{+3100}_{-1000}$	$.0008 \pm .0005$	2.84
		Exponential Disks, R00 halo II ( $\frac{c}{a} = .60, n = 2.75$ )					
$0.0047 \pm .0012$	280	$2100^{+10000}_{-700}$	$0.084 \pm .0018$	$740 \pm 50$	$3900^{+3400}_{-1000}$	$.0013 \pm .0007$	2.70
		Exponential Disks, N97 halo ( $\frac{c}{a} = 1.0, n = 3.0$ )					
$0.0046 \pm .0011$	280	$1700 \pm ^{+2500}_{-500}$	$0.070 \pm .014$	$850 \pm 60$	$4800 \pm ^{+4900}_{-1300}$	$.0004 \pm .0003$	3.28
		Exponential Disks, B99 halo ( $\frac{c}{a} = .85, R_e = 2.69$ kpc)					
$0.0047 \pm .0011$	280	$1800 \pm ^{+3200}_{-500}$	$0.068 \pm .013$	$860 \pm 60$	$4800 \pm ^{+4500}_{-1300}$	$.0004 \pm .0004$	3.25

Scaleheights not corrected for binarism.

Table 4. Best Fit for Exponential Disks, Flattened  $R_G^{-2.75}$  Halo

Cut	$\rho_{thin}$ ( $pc^{-3}$ )	$Z_{0,thin}$ ( $pc$ )	$R_{0,thin}$ ( $pc$ )	$\rho_{thick}$ ( $\rho_{thin}^{-1}$ )	$Z_{0,thick}$ ( $pc$ )	$R_{0,thick}$ ( $pc$ )	$\chi^2$
$5.8 \leq R - I < 6.8$	$0.0047 \pm .0012$	$280 \pm 20$	$2100^{+10000}_{-700}$	$0.084 \pm .018$	$740 \pm 50$	$3900^{+3400}_{-1000}$	2.70
$6.8 \leq M_R < 7.8$	$0.0046 \pm .0010$	$275 \pm 20$	$2300^{+8000}_{-900}$	$0.083 \pm .013$	$900 \pm 70$	$3600^{+1800}_{-800}$	1.91
$7.8 \leq M_R < 8.8$	$0.0058 \pm .0008$	$295 \pm 15$	$2400^{+2100}_{-700}$	$0.027 \pm .007$	$1560^{+420}_{-330}$	$2400^{+2100}_{-700}$	1.83
$8.8 \leq M_R \leq 10.2$	$0.0143 \pm .0009$	$355 \pm 10$	$2350^{+1800}_{-500}$	$0.013 \pm .009$	$6200^{+\infty}_{-5500}$	$7000^{+\infty}_{-6000}$	2.18

Scaleheights not corrected for binarism.

Table 5. Best Fit for  $sech^2$  Disks, Flattened  $R_G^{-2.75}$  Halo

Cut	$\rho_{thin}$ ( $pc^{-3}$ )	$Z_{0,thin}$ ( $pc$ )	$R_{0,thin}$ ( $pc$ )	$\rho_{thick}$ ( $\rho_{thin}^{-1}$ )	$Z_{0,thick}$ ( $pc$ )	$R_{0,thick}$ ( $pc$ )	$\chi^2$
$5.8 \leq M_R < 6.8$	$0.0025 \pm .0007$	$230 \pm 20$	$3700^{+infty}_{-2200}$	$0.097 \pm .020$	$570 \pm 40$	$3000^{+1700}_{-600}$	2.73
$6.8 \leq M_R < 7.8$	$0.0023 \pm .0005$	$240 \pm 20$	$2700^{+\infty}_{-1100}$	$0.079 \pm .011$	$780 \pm 50$	$3600^{+1500}_{-700}$	2.28
$7.8 \leq M_R < 8.8$	$0.0032 \pm .0005$	$230 \pm 10$	$2600^{+4800}_{-1000}$	$0.053 \pm .009$	$860 \pm 110$	$2400^{+1200}_{-500}$	1.59
$8.8 \leq M_R \leq 10.2$	$0.0085 \pm .0006$	$255 \pm 10$	$2600^{+1400}_{-800}$	$0.045 \pm .012$	$3800^{+\infty}_{-3000}$	$2500^{+\infty}_{-1200}$	1.89

Scaleheights not corrected for binarism.

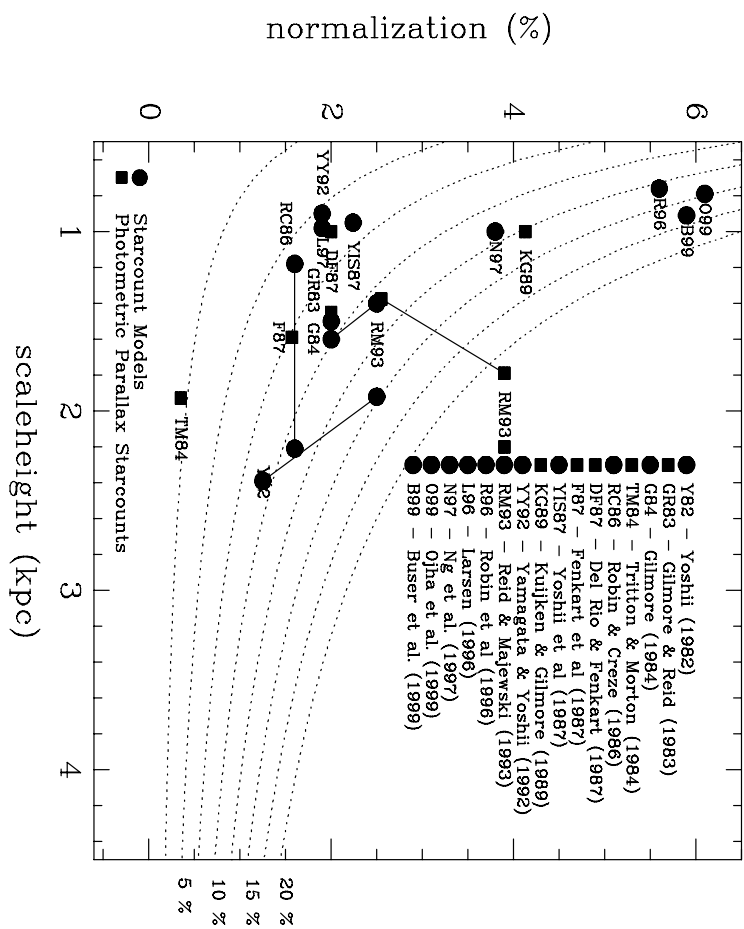
Table 6. The New Model

Parameter	Value	Corrected Value <sup>a</sup>
$Z_{0,thin}^b$	280 pc	350 pc
$Z_{0,thin}^c$	230 pc	290 pc
$R_{0,thin}$	2-2.5 kpc	
$\rho_{thick}$	6-10%	
$Z_{0,thick}^b$	700-1000 pc	900-1200 pc
$Z_{0,thick}^c$	500-800 pc	600-1000 pc
$R_{0,thick}$	3-4 kpc	
$\rho_{halo}$	.15%	
$\frac{c}{a}$	0.5-0.7	

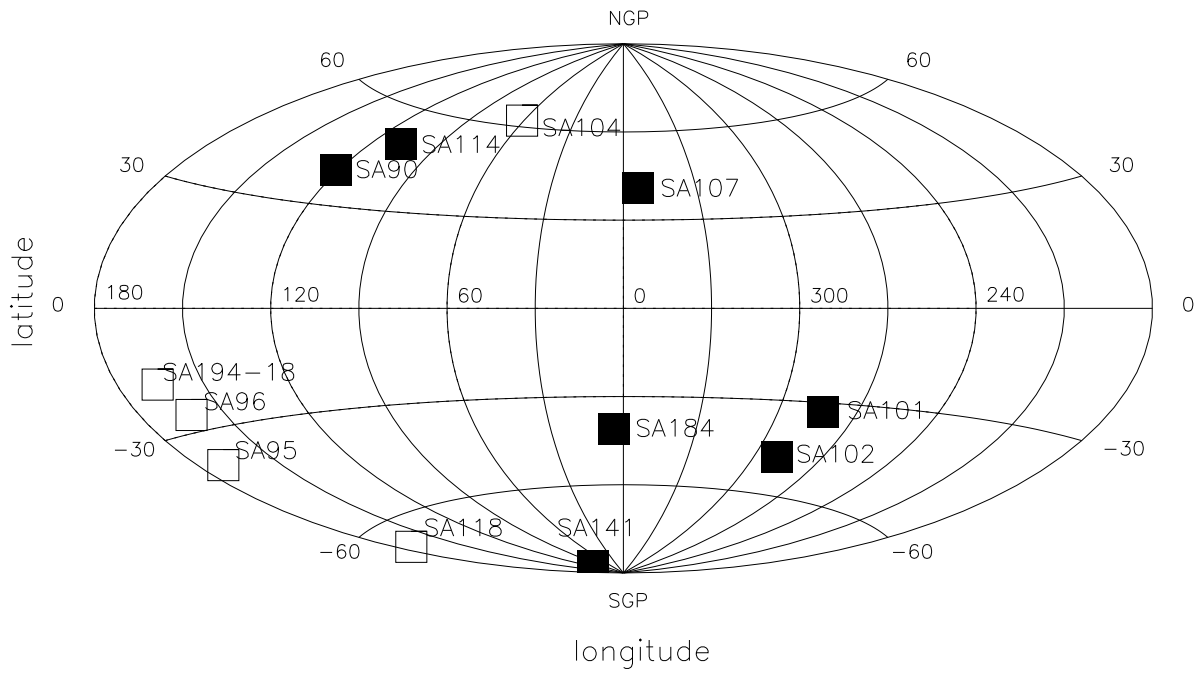
<sup>a</sup>Scaleheights corrected for binarism with 50% binary fraction.

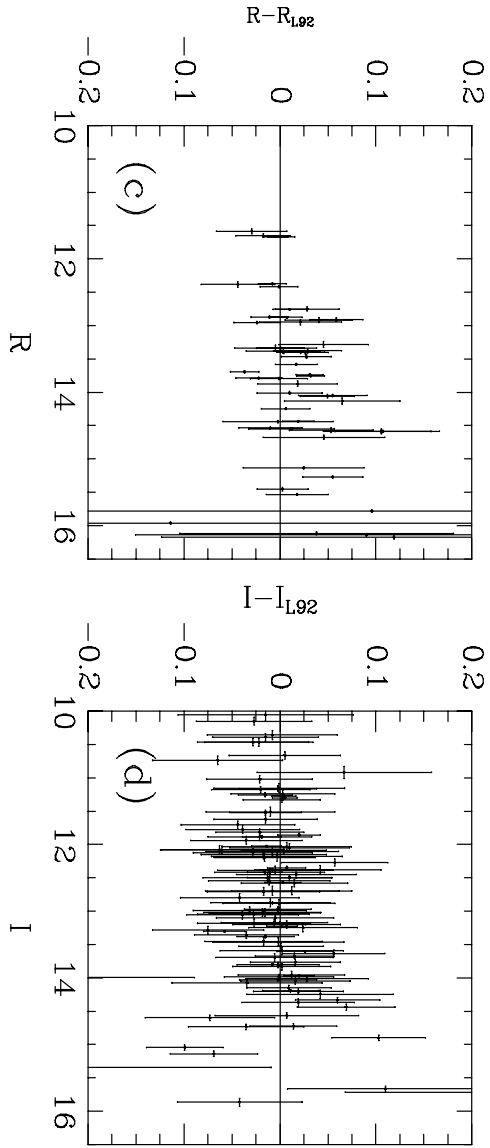
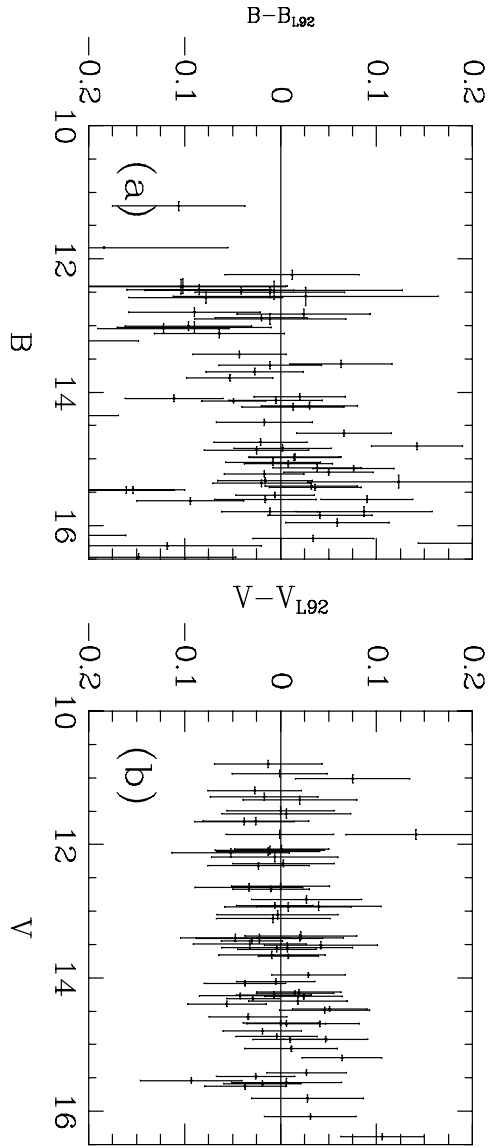
<sup>b</sup>Exponential Scaleheight

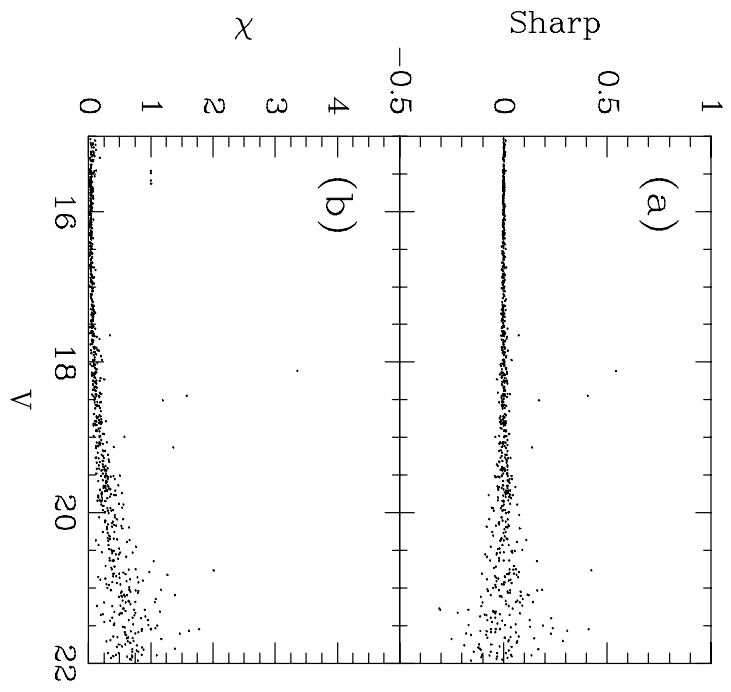
<sup>c</sup> $sech^2$  Scaleheight

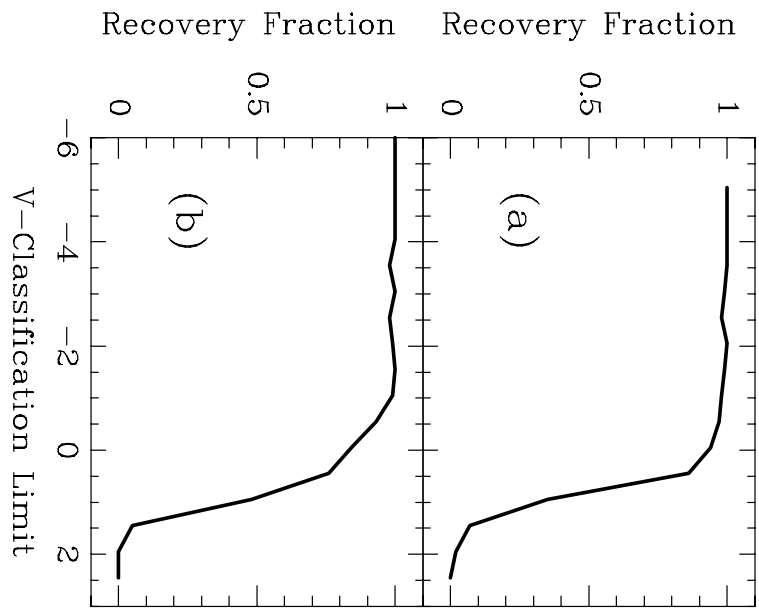


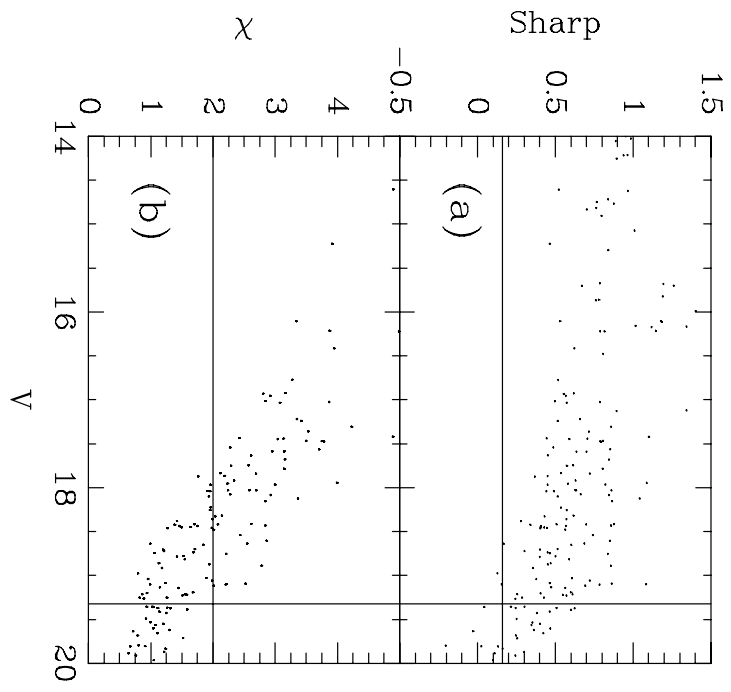


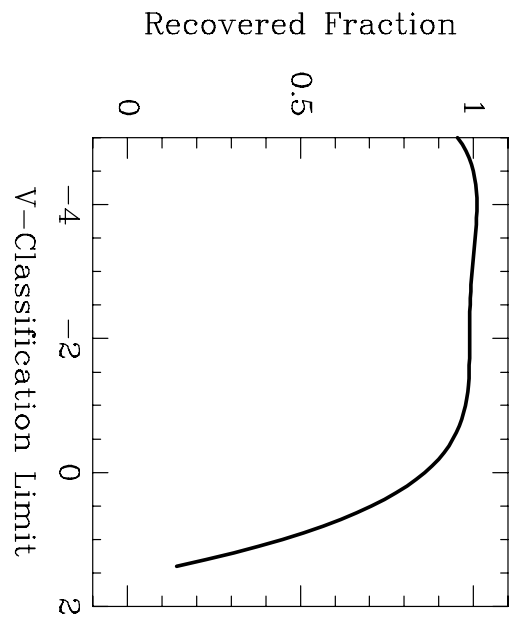


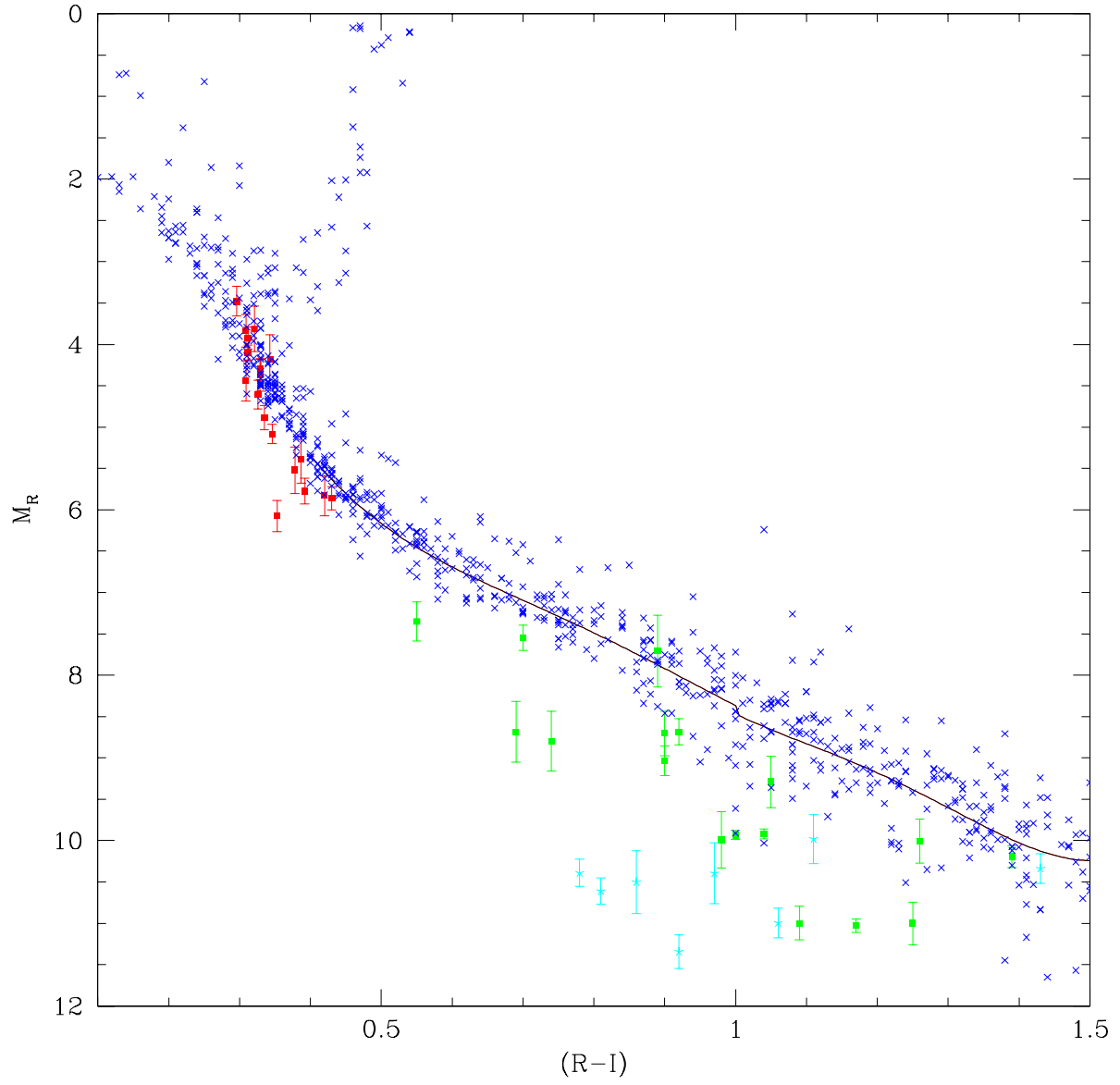


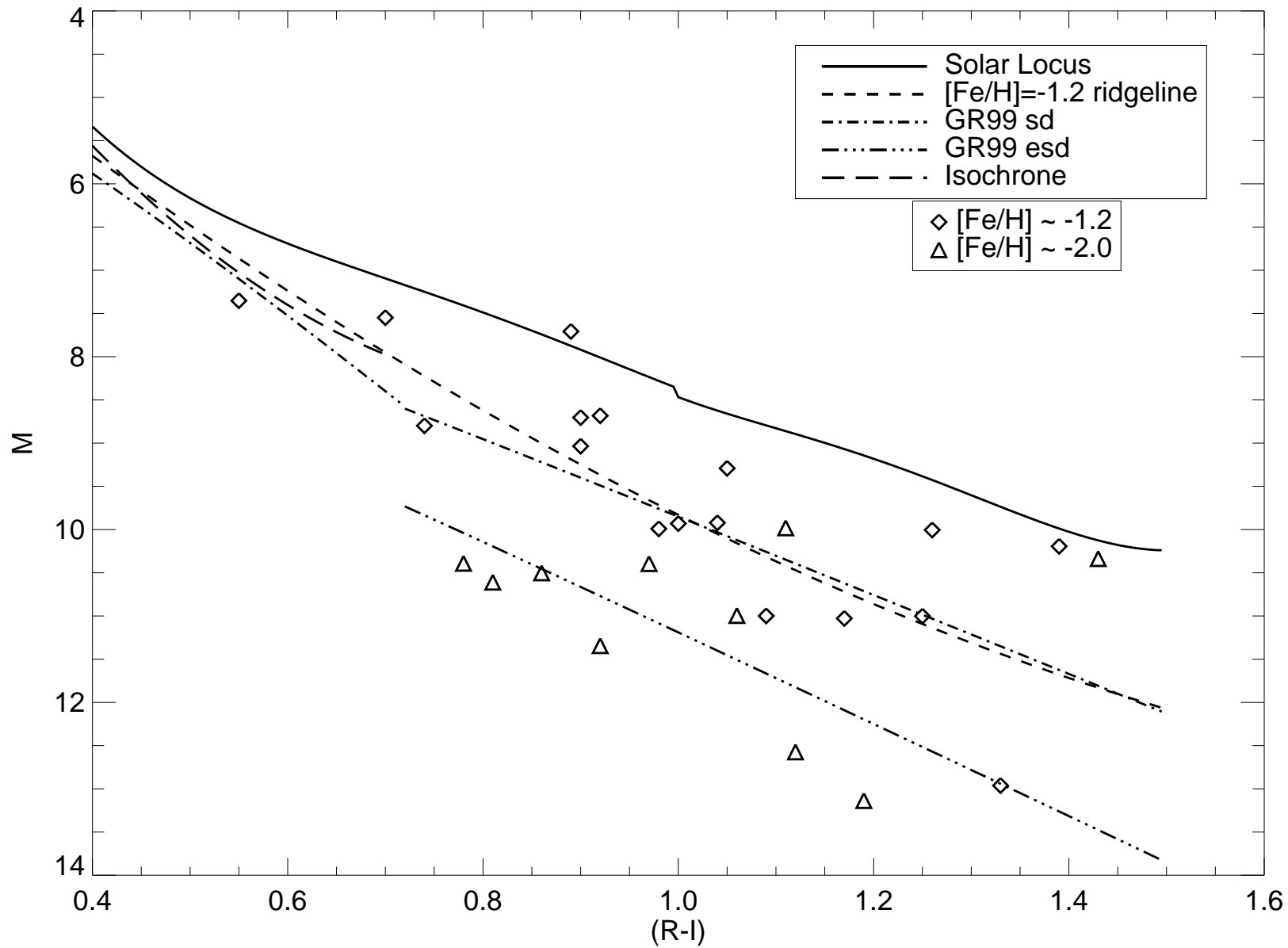




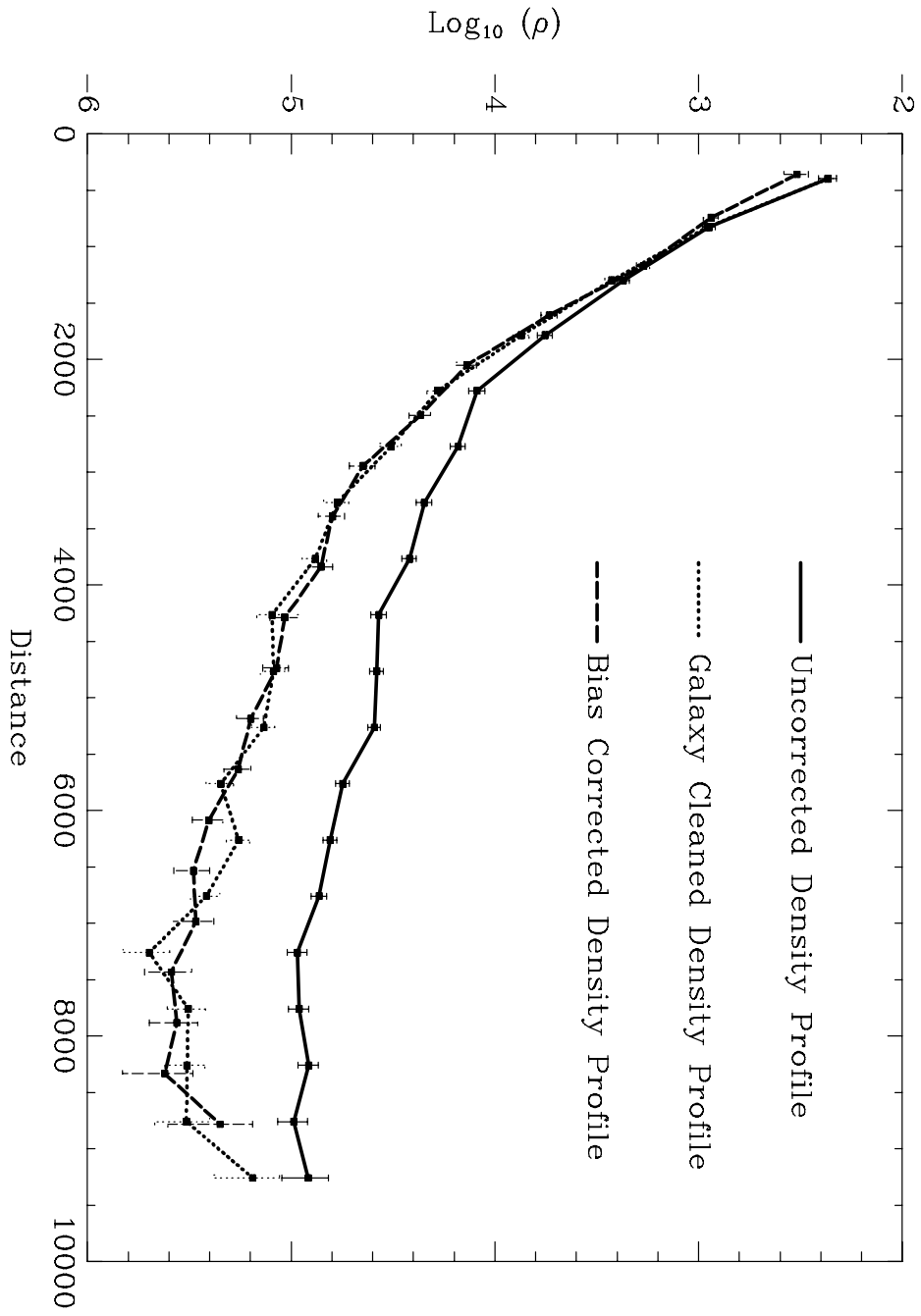




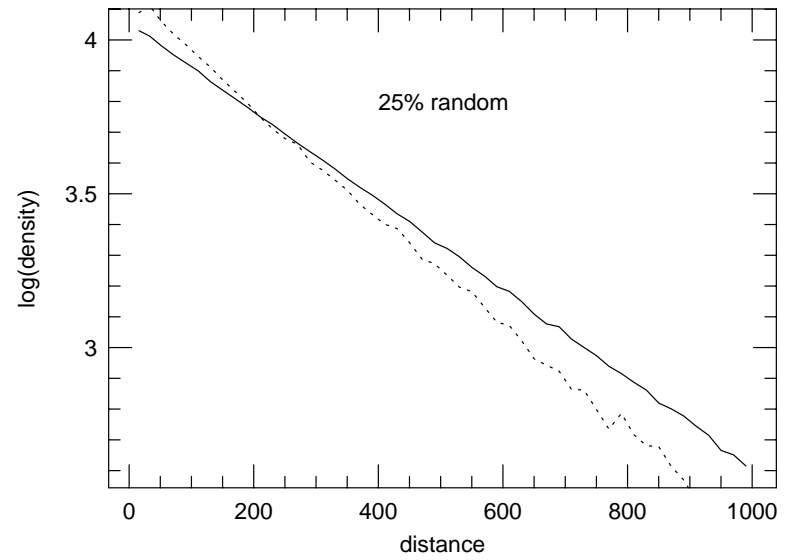
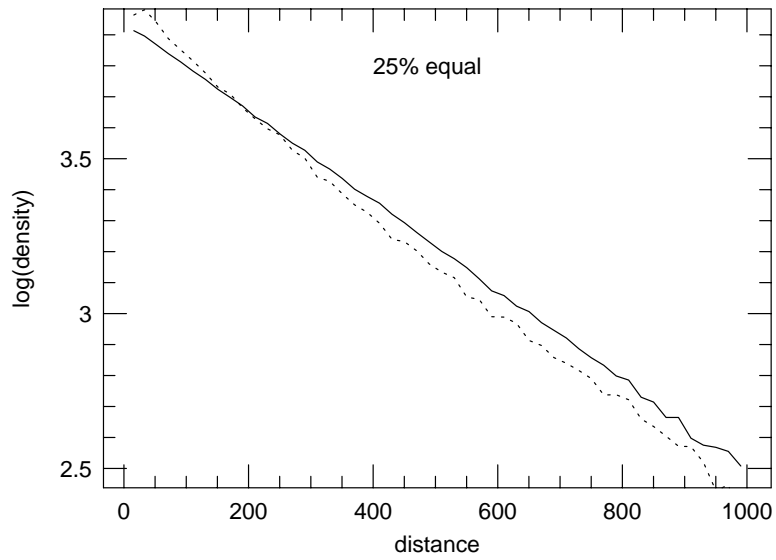
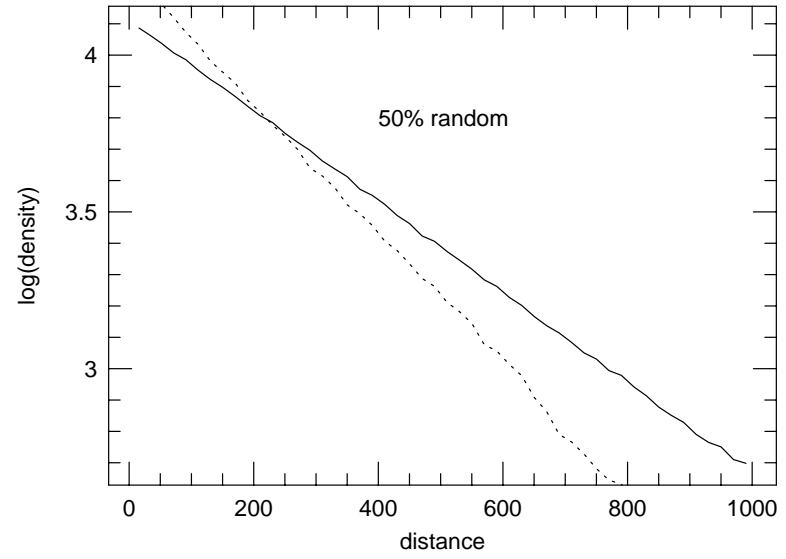
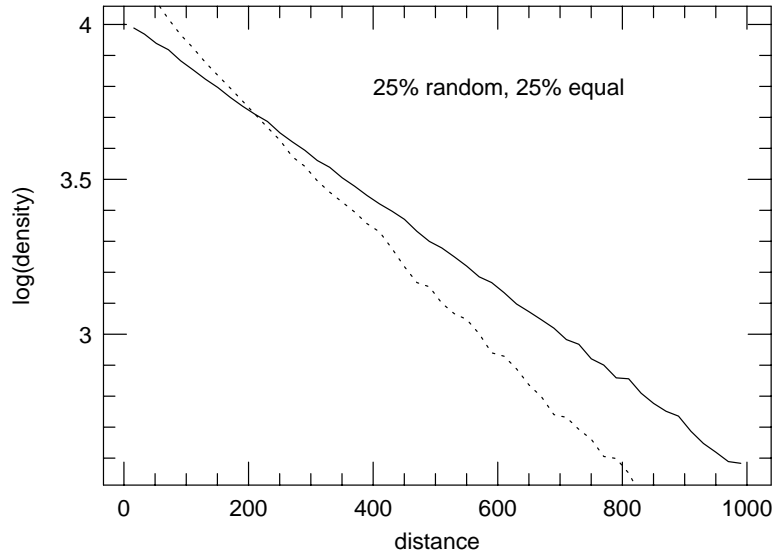


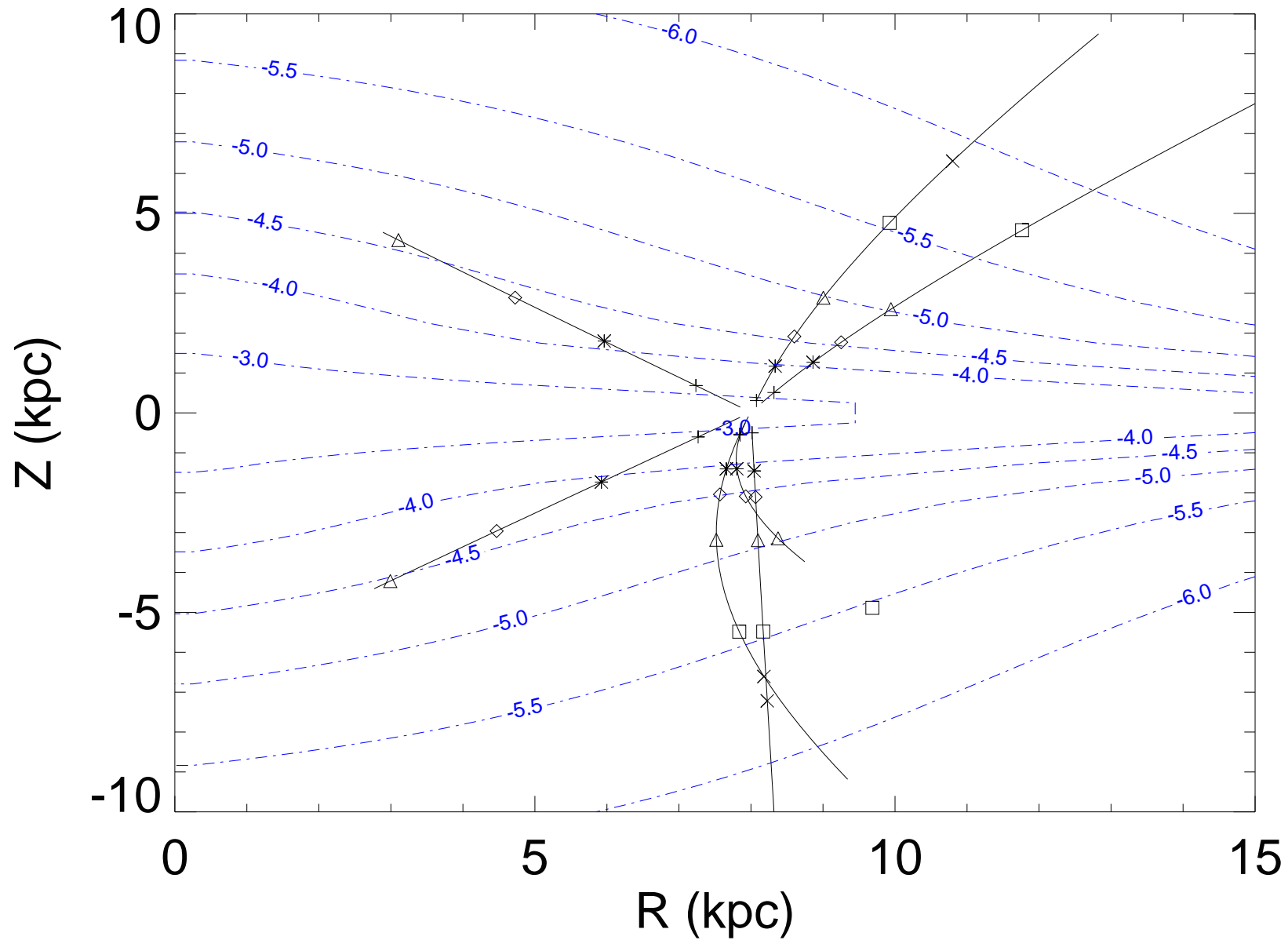


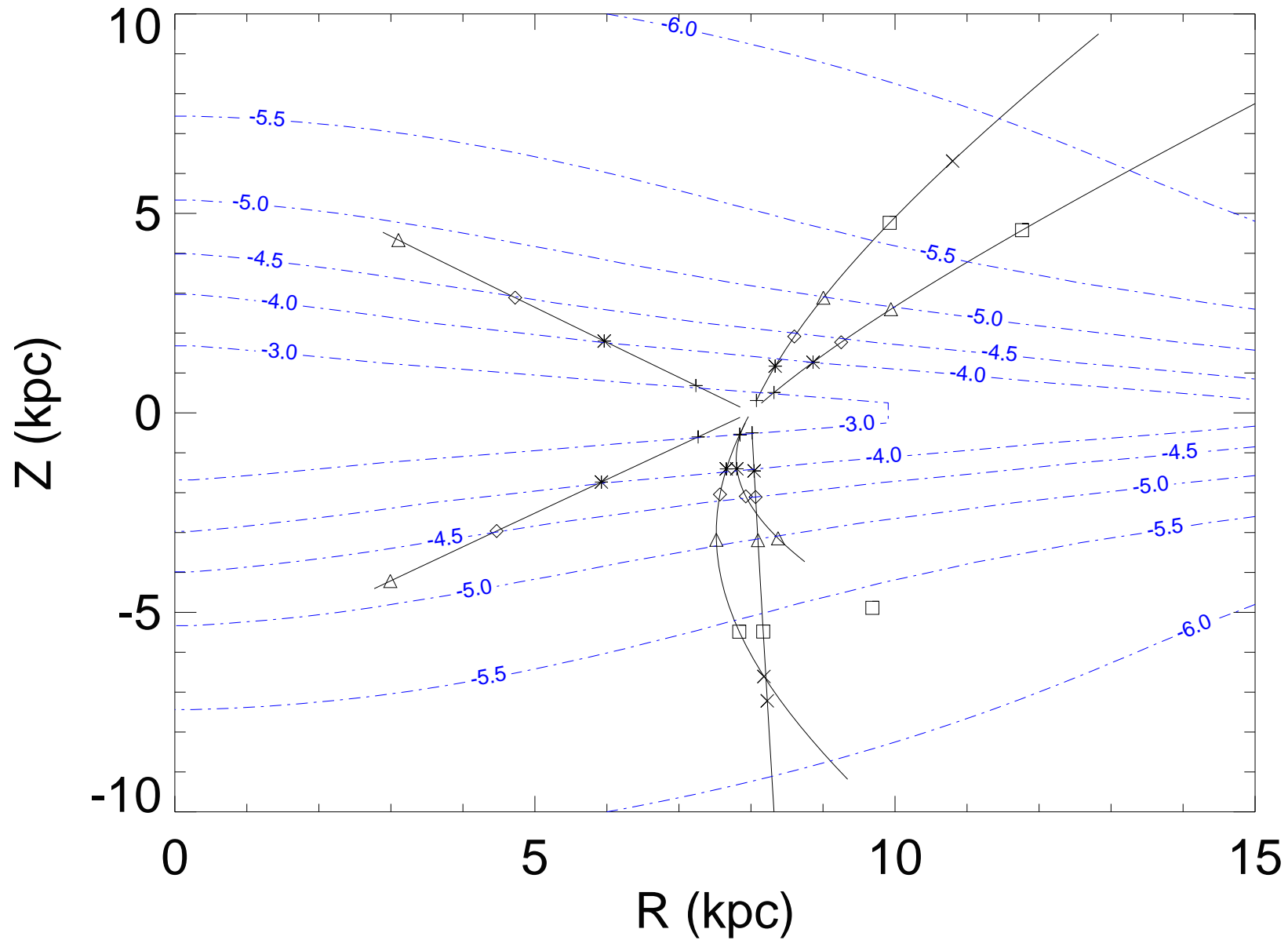


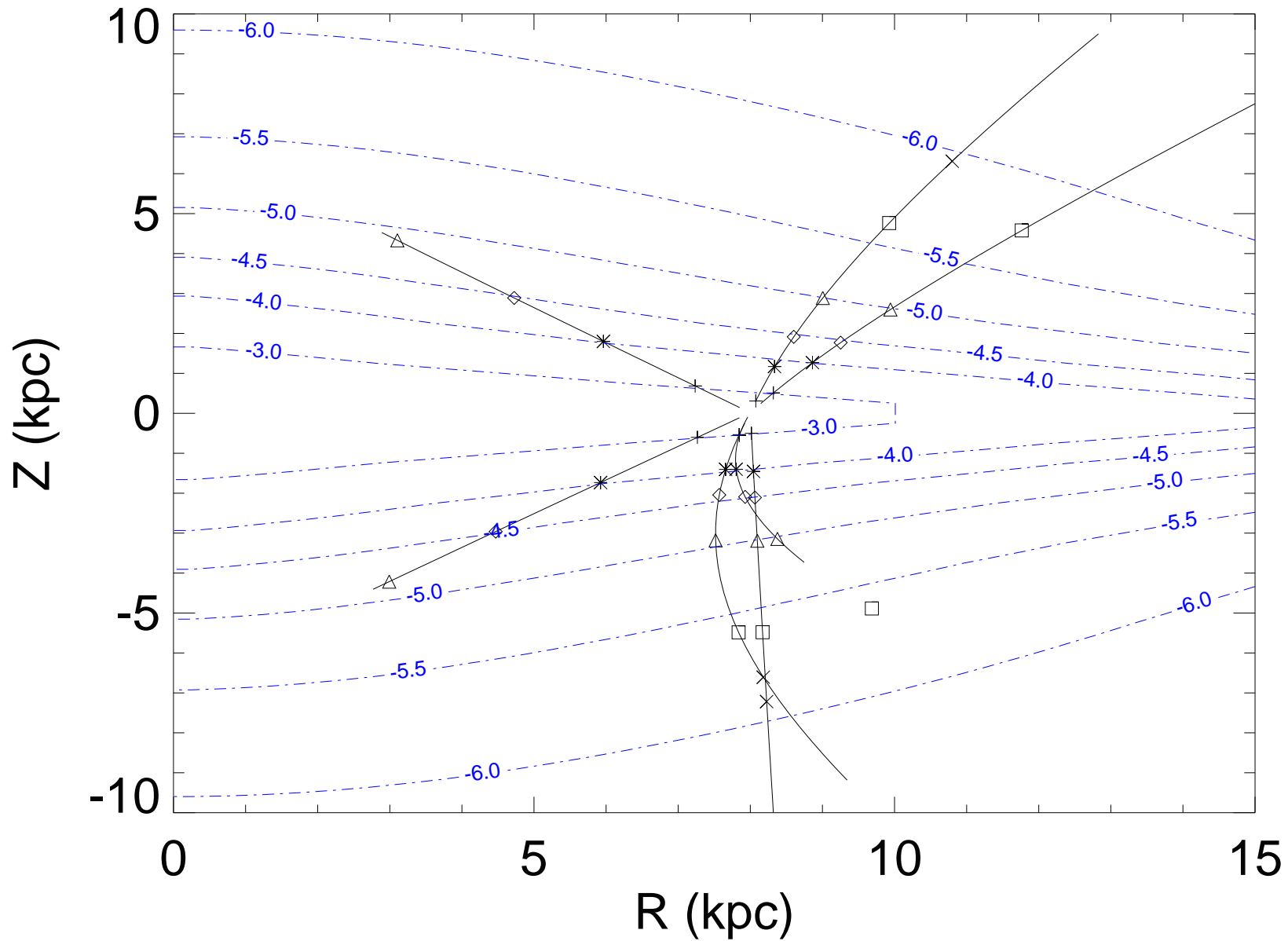


# Effect of binaries on photometric $\rho(z)$









This figure "f4.jpg" is available in "jpg" format from:

<http://arxiv.org/ps/astro-ph/0206323v1>

This figure "f5.jpg" is available in "jpg" format from:

<http://arxiv.org/ps/astro-ph/0206323v1>

This figure "f6.jpg" is available in "jpg" format from:

<http://arxiv.org/ps/astro-ph/0206323v1>



This figure "f10.jpg" is available in "jpg" format from:

<http://arxiv.org/ps/astro-ph/0206323v1>

This figure "f12.jpg" is available in "jpg" format from:

<http://arxiv.org/ps/astro-ph/0206323v1>